

Functional Connectivity Dynamics of the Resting State across the Human Adult Lifespan

Authors: Demian Battaglia^{1*}, Thomas Boudou^{1,2}, Enrique C. A. Hansen^{1,3}, Sabrina Chettouf^{4,5,6,7}, Andreas Daffertshofer⁷, A. Randal McIntosh⁸, Joelle Zimmermann^{4,8}, Petra Ritter^{4,5,6,9} + and Viktor Jirsa¹ +

Affiliations:

¹Université Aix-Marseille, INSERM UMR 1106, Institut de Neurosciences des Systèmes, F-13005 Marseille, France;

²ENSTA ParisTech, F-91762 Palaiseau, France;

³Frankfurt Institute for Advanced Studies, D-60438 Frankfurt am Main, Germany;

⁴Department of Neurology, Charité Universitätsmedizin, D-10117 Berlin, Germany;

⁵Bernstein Focus State Dependencies of Learning and Bernstein Center for Computational Neuroscience, D-10117 Berlin, Germany;

⁶Minerva Research Group BrainModes, Max Planck Institute for Human Cognitive and Brain Sciences, D-04103 Leipzig, Germany;

⁷Faculty of Behavioural and Movement Sciences, Vrije Universiteit Amsterdam, 1081 BT Amsterdam, The Netherlands;

⁸Rotman Research Institute, Baycrest Centre, Toronto, Ontario, M6A 2E1, Canada;

⁹Berlin School of Mind and Brain & Mind and Brain Institute, Humboldt University, D-10117 Berlin, Germany.

+Shared last authorship

*Corresponding author and lead contact:

Demian Battaglia (demian.battaglia@univ-amu.fr)

Keywords:

Functional Connectivity Dynamics | Resting State | fMRI | Aging | Cognitive aging

Abstract

The aging brain undergoes alterations of both Structural Connectivity (SC) and time-averaged Functional Connectivity in the resting state (rs FC). Here, we show by means of functional MRI (fMRI) human brain imaging that aging also profoundly impacts on the spontaneous temporal reconfiguration of this rs FC. Analyzing time-dependent correlations between human rs fMRI blood oxygen level dependent (BOLD) time series, we describe Functional Connectivity Dynamics (FCD) as a switching between epochs of meta-stable FC and transients of fast network reconfiguration. We find that the flux of FCD markedly slows down and becomes more “viscous” across the adult lifespan (18-80 yrs), also accounting for the wide inter-subject variability of performance observed in cognitive screening tasks. Such remodeling of FCD discloses qualitatively novel effects of aging that cannot be captured by variations of SC or of static FC, opening the way to improved imaging-based characterizations of the functional mechanisms underlying cognitive aging.

Highlights

- Functional Connectivity Dynamics (FCD) at rest performs an anomalous random walk.
- The speed at which the flux of FCD unrolls in time slows down with aging.
- The “viscosity” of FCD grows, correlating with subject-specific cognitive fluency.
- FCD methods are complementary to structural and functional connectivity analyses.

Short summary

Battaglia et al. show that aging affects Functional Connectivity Dynamics (FCD) in the resting state. Analyzing human fMRI data, they find that the flux of FCD slows down and becomes more “viscous” through aging, predicting inter-subject differences in cognitive performance.

Introduction

As we age, our brain undergoes structural and functional changes. Tractographic studies revealed a tendency toward cortical ‘disconnection’, as manifested by an age-related decline in white matter integrity (O’Sullivan et al., 2001; Salat, 2011). These decreases in structural connectivity (SC) are paralleled by disruptions of resting state (rs) functional connectivity (FC). Inter-regional BOLD correlations are reduced within rs networks (RSNs) such as the Default Mode or the Dorsal Attentional networks (Andrews-Hanna et al., 2007; Ferreira & Busatto, 2013), implicated in attention, memory and executive control functions, which decline in cognitive aging (Castel & Craik, 2003; Buckner, 2004). However, changes in rs FC are not just reflecting SC changes. For instance, FC between RSNs tends to increase with age (Betz et al., 2014; Geerligs et al., 2015). The correlation between SC and FC may either increase or decrease depending on the considered region and these variations in SC-FC coupling predict age better than SC or FC alone (Zimmermann et al., 2016). Here, we show that aging not only affects rs FC but also its spontaneous reconfiguration over time, i.e. Functional Connectivity Dynamics (FCD).

Recent studies emphasized the structured temporal variability of rs FC (Tagliazucchi et al., 2012; Allen et al., 2012; Liu & Duyn, 2013; Hutchison et al., 2013a-b; Chen et al., 2015), whose study is the defining focus of a research direction recently designated as “chronnectomics” (Calhoun et al., 2014). If rs FC is dynamic, a wealth of information may be lost by averaging over long imaging sessions. Averaged temporal variability might be mistaken as inter-subject variability. Furthermore, temporal FC variability may carry an inherent meaning, by manifesting ongoing cognition at rest (Gonzalez-Castillo et al., 2015) with a direct impact on cognitive performance (Bassett et al., 2011; Shine et al., 2016) or by reflecting the sampling of a repertoire of dynamical states (Hansen et al., 2015). From a biomarking perspective, pathological conditions, such as Alzheimer’s dementia or schizophrenia (Jones et al., 2012; Damaraju et al., 2014), or differences in general attributes like gender or developmental stage (Yaesoubi et al., 2015; Hutchison & Morton, 2015), may alter FCD more than they affect time-averaged FC.

Using a homogeneous brain imaging data set including $N = 85$ healthy human adult subjects (between 18 and 80 yrs), we quantified age-related variations in the rate of reconfiguration of FC networks – ‘speed’ of FCD – and describe the spatio-temporal coordination patterns (*meta-connectivity*) that constrain the time-variability of FC links. We found that the flux of FCD at the whole cortex level markedly slows down with age and that it becomes more ‘viscous’, i.e. with the smooth and free FC reconfiguration increasingly frustrated by conflicting inter-link influences. FCD-based markers were also predictive of individual differences in cognitive performance between subjects of similar age, as probed by both standard clinical assessments of cognitive impairments (Nasreddine et al., 2005) and a simple visuomotor coordination task (Houweling et al., 2008). This capacity of tracking cognitive performance hints at the relevance of FCD for actual mental operations, where, speculatively, the slowing down of FCD may provide a brain imaging counterpart to the general reduction in information processing speed postulated by classic theories of cognitive aging (Salhouse, 1996; Finkel et al., 2007).

Results

Aging slows down Functional Connectivity Dynamics. A widespread manner to extract FC from rs fMRI is to parcellate the brain into N macroscopic regions – see Table 1 and Desikan et al. (2006) – and to compute pairwise correlations between the

region-averaged time series of neural activity a_p , based on the entire rs imaging session (tens of minutes). The result of this procedure is an N -times- N FC matrix (Fig. 1A), whose spatial structure is reminiscent of the underlying N -times- N SC matrix, shown for comparison in Fig. S1A (Honey et al., 2009; Hansen et al., 2015). In order to go beyond static, time-averaged FC and estimate the time dependency of FC, we adopted a common sliding window approach – followed e.g. by Allen et al. (2012) –, repeating the FC construction separately for each time-window (of a fixed duration τ). By this we generated a stream of $FC(t)$ matrices (Fig. 1B) and studied the similarity between different time-resolved networks. To do so, we introduced a metric of similarity between FC matrices and evaluated *Functional Connectivity Dynamics* (FCD) matrices (Hansen et al., 2015). The FCD matrix entries FCD_{ab} provide the normalized correlation $CC[FC(t_a), FC(t_b)]$ between any two $FC(t)$ networks observed at times t_a and t_b .

Fig. 2A shows FCD matrices for subjects of different ages (see Fig. S2 for different τ -s). $FC(t)$ matrices were stable during epochs lasting several time windows, as visualized in Fig. 2A by square-shaped red blocks along the main FCD matrix diagonal, denoting high similarity between $FC(t)$ networks within the epoch. Such epochs of transient FC stability – or ‘FCD knots’ – often terminated abruptly, and were intertwined with transients of instability, visualized in Fig. 2A by bluish stripes in the FCD matrix, denoting strong dissimilarity from previously visited $FC(t)$ networks. During these transients – or ‘FCD leaps’ – $FC(t)$ quickly morphed before stabilizing again into the next FCD knot. Note that the alternation between FCD knots and leaps does not imply the existence of crisply separated FC states (see *Discussion*). The typical duration of FCD knots depended on subject age. As shown by Fig. 1A, FCD in older subjects seemed to slow down with respect to younger subjects, as revealed by longer lasting FCD knots.

To provide a quantitative description of the slowing down of FCD, we provided a statistical characterization of the rate of stochastic change in time of rs FC networks. We described the dynamics of FC as a stochastic exploration of the space of possible FC configurations. We sampled $FC(t)$ at discrete times $t_0, t_1 = t_0 + \tau, \dots, t_k = t_0 + k\tau, \dots$ and evaluated the lengths of the steps traveled in FC space between each of these ‘stroboscopic’ observations. We measured step lengths as the correlation distance between two consecutive $FC(t)$ networks, i.e. $d_t[t_i] = 1 - CC[FC(t_i), FC(t_i + \tau)]$. In this way, FCD step lengths are large when two consecutive $FC(t)$ observations are poorly correlated (as within a FCD leap) and close to zero when two consecutive $FC(t)$ observations are highly correlated (as within a FCD knot). These measured d_t can also be interpreted as describing a *speed of FCD reconfiguration*, since consecutive $FC(t)$ observations were always separated by the same amount of time τ . We sampled the statistical distributions of d_t for different ranges of τ and different subjects (see *Methods*). Distributions of d_t for two representative subjects of different ages are shown in Fig. 2B. For all considered τ -s and subjects (see also group averages in Fig. S3A and different τ -s in Fig. S3B), these distributions displayed a peak at a value d_{typ} , which we call the *typical FCD speed*. As shown in Fig. 2C, d_{typ} significantly decreased with age ($-0.74 < R_{50} = -0.58 < 0.44$, 99% bootstrap c.i.), thus confirming our intuition.

For the analyses underlying Figs. 2B-C, we used a range of time scales (pooled windows sizes from 31 to 12 s), which is unusual and relatively very fast when dealing with BOLD signals. If the adoption of such short window-sizes introduced a large noise in the estimation of the spatial structure of individual $FC(t)$ matrices, it nevertheless allowed probing their temporal variability in a more regular way, by extracting longer d_t sequences and thus improving the estimation of d_t distributions at the single subject level

(see *Discussion*). The same trend was confirmed as well for larger, more standard τ -s, but age correlations were in this case weakened, although still significant (Fig. S3B).

Functional Connectivity Dynamics is an anomalous stochastic process. The sampled FCD speed distributions had a second property. Their left tail had a slow decay (red distributions in Fig. 2B) and was significantly fatter than chance expectations (grey distributions in Fig. 2B), evaluated under the null hypothesis of no sequential correlations between consecutive steps in the $FC(t)$ stream (removed by random shuffling of the order within the stream). Such over-representation of short step lengths d_t was consistently observed across all subjects and τ -s (Fig. S3C) and is due to the fact that $FC(t)$ networks transiently stabilized within FCD knots. Their speed of reconfiguration was thus reduced to only increase again when a FCD knot ‘melted’ into a FCD leap. The graphical cartoons in Fig. 2D visualize our interpretation of the phenomenon. The FC sequences in experimental data, alternating between short steps within FCD knots and longer steps during FCD leaps (Fig. 2D, top), bear analogies with anomalous stochastic processes showing *persistence* – i.e., long-lasting sequential auto-correlations of increments – such as Lévy flights (Mandelbrot, 1983; Metzler et al., 2014). The resulting FCD trajectories contrasted with the null hypothesis of vanishing sequential correlations between step lengths (Fig. 2D, bottom) in which the trajectories would spread homogeneously over the same volume in FC space.

We rigorously confirmed that FCD instantiate an anomalous stochastic process by performing a Detrended Fluctuation Analysis (DFA) of the sequences of d_t , supplemented by a (Bayesian) model-selection step (Ton & Daffertshofer, 2016). This robust procedure quantifies the strength of auto-correlations in a sequence by detecting a power-law scaling – described by a scaling exponent α_{DFA} – in the divergence of a quantity $\langle F_q(k) \rangle$, probing the strength of the fluctuations of d_t at different scales of observation k (see *Methods*). A value of $\alpha_{\text{DFA}} = 0.5$ corresponds to a Gaussian white noise process, in which the expected fluctuation after N uncorrelated steps grows as \sqrt{N} . In contrast, larger values $0.5 < \alpha_{\text{DFA}} \leq 1$ correspond to so-called *fractional Gaussian noise* which is anomalously persistent ($\alpha_{\text{DFA}} = 1.0$ corresponding to a Lévy walk). Model comparison allows for discarding subjects for which a genuine power-law scaling is not present (Ton & Daffertshofer, 2016).

Fig. 2E shows DFA log-log plots for two representative subjects (based on a FCD analysis with a short $\tau = 12$ s). The slopes of the straight lines fitted to $\log\langle F_q(k) \rangle$ provide an estimate of α_{DFA} . For all window-sizes up to $\tau < 29$ s, at least 70% of the tested subjects showed a genuine power-law scaling of $\langle F_q(k) \rangle$, according to (Bayesian) model selection (for $\tau = 12$ s, $N = 46$ out of 49 subjects). For all of them, α_{DFA} was significantly larger than 0.5 ($p < 0.05$, bootstrap c.i.). The median α_{DFA} was closer to 1.0 for elderly than for younger subjects (Fig. 2F). We also found a significant positive correlation between α_{DFA} and age at the single subject level (Fig. S4A), robustly up to window sizes of $\tau \sim 29$ s. (Figs. S4B–C). For longer τ -s – and correspondingly shorter d_t sequences –, correlations were no longer significant.

Aging reduces the temporal stability of functional connectivity modules. The slowing-down of FCD is not necessarily paralleled by an enhanced temporal stability of the topology of time-resolved FC networks. We studied in particular how the modular structure of $FC(t)$ varied across time, as an effect of ongoing rs FCD. We first separately partitioned each of the $FC(t)$ networks into non-overlapping graph modules, using a standard community detection algorithm. Since the obtained modules were generally not identical in different time-windows, we re-clustered them across time-slices (see *Methods*)

in order to maximize the window-to-window overlap between matched modules. We could thus track when brain regions were changing modular class, transiting toward a different community than the one they belonged to at a previous time.

A dynamic community analysis of the $FC(t)$ stream is shown in Fig. 3. In Fig. 3A (top) the time-dependent modular membership of different brain regions is color-coded. For the shown representative subject, the sampled $FC(t)$ networks could contain up to five different modules, and the number of detected modules fluctuated in time. At every time step we quantified the ‘liquid fraction’ $\Lambda(t)$ of regions, i.e. the fraction of regions within each module transiting to a different module at the next time step. We found that the average number of detected modules decreased with age (Fig. 3B) and that the average liquid fraction $\bar{\Lambda}$ within a module increased with age (Fig. 3C). Thus, the ongoing rs FCD had on elderly subjects a more destabilizing effect on the modular structure of the $FC(t)$ networks, despite its slowing down.

Our results are in agreement with an independent study by Schlesinger et al. (2016) which also found an enhanced temporal flexibility of FC modules in the elderly, as we do in Fig. 3C. However, Schlesinger et al. (2016) report an increasing number of modules, in contrast with our Fig. 3B. This discrepancy is of a technical nature, due to the different clustering procedures adopted in the two studies (see *Methods*).

Aging increases the viscosity of Functional Connectivity Dynamics. To reveal further age-related effects, we introduced an alternative characterization of FCD. We converted the $FC(t)$ stream of Fig. 1B into a collection of time series describing the time-dependency of individual FC pairwise couplings (Fig. 1C). By extending the FC matrix construction from regional nodes to inter-regional links, we built a $N(N-1)$ -times- $N(N-1)$ matrix of correlations between the time-dependent strengths of $N(N-1)$ FC links (N^2 pairs of regions, minus the self-loops). The resulting matrix—which we rebaptized *Meta-Connectivity (MC)*—described inter-link covariance, similarly to FC describing inter-node covariance. MC matrices are particularly suitable for inter-group comparisons. In fact, they can be averaged over multiple subjects within a homogeneous group (expected to share common inter-link correlations), while this cannot be done for FCD matrices (portraying specific realizations of FC fluctuations, different for each subject in a group).

MC captures higher-order correlations between triplets or quadruplets of brain regions, beyond pairwise FC. Indeed, estimating the strength of a *meta-link* $MC_{ij,kl}$ between two functional links FC_{ij} and FC_{kl} requires monitoring the coordinated activity of minimum three brain region (for *MC trimers*, when the two links share a common root region, $i = k$) or, generally, four (for *MC tetramers*, when the two links do not share any vertex). Thus MC analysis tracks the static high-order correlation structures, as previously pointed out (Davison et al., 2015), which shape the coordinated stochastic fluctuations of second-order pairwise FC.

Fig. 4A shows average MC matrices for different age groups, based (here and in the following) on sliding FCD windows of $\tau = 31$ s. Both these MC matrices exhibited a modular structure, characterized by communities of temporally co-varying FC links. In Fig. 4A, in order to better emphasize this modular structure with respect to Fig. 1C, we have reordered rows and columns according to their membership to different MC modules. For each individual MC module, Fig. 4B displays a cortical map of the associated trimer weights $MC(i)$, i.e. of the sum of the weights of trimer meta-links $MC_{ij,il}$ belonging to a given MC module and being rooted in a region i . These maps (averaged over the two hemispheres, given the absence of large asymmetries) allow to visualize *meta-hub* regions with elevated $MC(i)$, around which the different modules are organized. While a conventional FC hub region is a network node whose activity fluctuations highly

correlate with those of adjacent nodes, a meta-hub region is characterized by a high degree of correlation between the fluctuations of its *incident FC links*. MC modules and the associated meta-hub regions characteristically distribute across the whole rostro-caudal range (Fig. 4B).

These modules do not overlap with the spatial extent of any standard RSN (Damoiseaux et al., 2006). We would like to remark that focusing on trimer meta-connectivity exaggeratedly emphasizes the localized nature of the MC modules. By considering all meta-links together – the majority of which were tetramers –, we found that every MC module ‘touched’ nearly every region through at least one meta-link (Fig. S5A). Hence, functional meta-networks formed pervasive higher-order correlation scaffolds that coordinate the temporal fluctuations of brain-wide FC networks.

A striking effect of aging on our MC results is the surfacing of negative meta-links, apparent from the darker blue hue of the elderly group MC matrix (Fig. 4A, right). The results in Fig. 4C revealed that, although the median strength of individual MC weights decreased for elderly subjects ($p < 0.001$, Kruskal-Wallis), the bulk of their distributions largely overlapped (blue 95% c.i. in Fig. 2C). Nevertheless, the elderly group’s distribution developed a tail of negative MC outlier entries (dashed red ranges in Fig. 4C). Negative meta-links were detected within and between all MC modules (Fig. S5B-C). At the single subject level, we defined as *FCD viscosity* the quantity *neg-MC*, given by the total absolute strength of all negative MC entries. We found that FCD viscosity grows significantly with age (Fig. 4D). A growing neg-MC tracks the emergence of a mixture of negative and positive interactions between different FC links. These conflicting actions and reactions result in a reduced freedom for links belonging to different MC modules to fluently follow independent ‘fluctuation choreographies’. In other words, the flux of FCD not only becomes slower with aging but also more clinging, more ‘viscous’ (hence the chosen name of FCD viscosity).

Functional Connectivity Dynamics predict cognitive performance. We were also interested in whether FCD alterations correlate with the age-related decline of cognitive and motor performance, which varies greatly between subjects of a same age group, and particularly among elderly subjects (Lindenberger & von Oertzen, 2006). We first related FCD to cognitive performance in a subset of old subjects between 60 and 70 yrs tested via the Montreal Cognitive Assessment (MoCA). MoCA is a standard cognitive screening tool for Mild Cognitive Impairment (Nasreddine et al., 2005), which recapitulates into a single global score the partial performances achieved in subtests for visuo-spatial abilities, language, orientation, attention, working memory and other executive functions.

The global MoCa score significantly correlated with the typical FCD speed d_{fp} (the faster the FCD, the better the score, Fig. 5A) and with neg-MC (the more viscous the FCD, the worse the score, Fig. 5B). We then considered performance in a simple unimanual visuo-motor coordination task, adapted from (Houweling et al., 2008). In this task, performance was measured, following (Daffertshofer et al., 2000), as the average frequency-locking – quantified by a coefficient $0 < \Phi < 1$ – between the rotations of two circles presented on a screen, a visual cue and a second, subject-generated, cyclic force (squeezing an air-filled rubber ball at certain frequency, see *Supporting Materials and Methods*). Once again, the correlations of Φ with d_{fp} (Fig. 5C) and with neg-MC (Fig. 5D) were significant (see Table 1).

Importantly, the correlations of the FCD speed d_{fp} and of the FCD viscosity neg-MC with performance indicators (MoCA or Φ) continued to be significant even when regressing out the common declining trend with age (see partial correlations, $CC(\cdot, \cdot |$

Age), in Table 1), showing that the large variability of FCD metrics within a common age class accounts for inter-subject variability in cognitive performance.

Among the partial MoCA scores, only the working-memory subtask score correlated significantly with neg-MC or d_{wp} (e.g. $CC(\text{neg-MC}, \text{MoCA-wm} \mid \text{Age}) = 0.65, p < 0.01$, bootstrap). The average liquid fraction $\bar{\Lambda}$ within $FC(t)$ modules weakly anti-correlated with the global MoCA score, but not with partial scores, and not at the level of partial correlations. DFA could not be performed on the subjects undergoing cognitive and motor performance assessment due to the shorter length of their rs fMRI scans.

Functional Connectivity Dynamics conveys new information. FCD speed and viscosity correlate with age, but many other features do it, such as SC (Fig. S1A), time-averaged FC (Fig. 1A), or even the variances $\sigma(FC)$ (Fig. S1B), capturing the fluctuation strengths of individual FC links, but not their covariance. We may thus ask whether FCD analyses really provide new information about the aging process, or, on the contrary, the age-related information carried by FCD is redundant with simpler or more traditional categories of predictors.

To identify possible redundancies, we attempted to predict the age of single subjects based on: just SC; just FC; just $\sigma(FC)$; just MC; a mix of features of the four different types. Not being interested in prediction performance by itself but rather on assessing the relative predictive power of the different feature types, we used a simple linear regression scheme, fitting a linear relation between age and the strengths of a set of predictive features on a training sub-sample –i.e., an age-balanced random split of the whole sample– and cross-validating the prediction error on a complementary testing sub-sample (see *Methods*). Considering all pairs of regions i and j , we tested as predictor sets all possible quadruplets of structural coupling strengths SC_{ij} , of time-averaged functional coupling strengths FC_{ij} and of their variances over time $\sigma(FC_{ij})$. We then considered quadruplets of link-integrated meta-connectivity strengths $MC(ij)$, i.e. sums of all the meta-links $MC_{ij,kl}$ converging on a fixed link $FC_{ij}(t)$. Finally, we also considered mixed quadruplets composed of exactly one feature of the SC_{ij} type, one of the FC_{ij} type, one of the $\sigma(FC_{ij})$ type and one of the $MC(ij)$ type. Note that we used integrated strengths $MC(ij) \sim N^2$ of them– rather than directly the ‘raw’ meta-connectivity matrix entries $MC_{ij,kl} \sim N^4$ of them–, to include the same number of predictors within each of the tested categories and thus compare them in a completely fair manner. Fig. 6A shows the cross-validated age prediction errors for the best quadruplet within each of the categories, and Fig. 6B-C report the specifically chosen highly performing quadruplets. For all the tested predictor categories we could achieve an age prediction error significantly below chance-level, confirming that all the categories convey age-related information. The best quadruplet of $MC(ij)$ predictors performed significantly better than the best quadruplets of SC_{ij} , FC_{ij} and $\sigma(FC_{ij})$ predictors ($p < 0.01$, Kruskal-Wallis with multiple comparisons correction). Importantly, the best quadruplet of mixed predictor types performed even better ($p < 0.05$, Kruskal-Wallis with multiple comparisons correction), hinting at the fact that different predictor types convey synergetic age-related information.

When systematically charting the correlations with age of distinct link features (cf. Fig. S6) we found indeed that it is difficult to anticipate whether, e.g., the strength of structural or functional links SC_{ij} and FC_{ij} also correlates with age when the integrated meta-connectivity strength $MC(ij)$ does. All possible scenarios were present. For instance: when $MC(ij)$ was anti-correlated significantly with age, sometimes SC_{ij} was anti-correlated, sometimes it was correlated (clouds of green dots in Fig. S6A) and some

other times it did not correlate at all (clouds of red dots). In other words, we could not identify any trivial pattern of redundancy between SC, FC, $\sigma(\text{FC})$ and MC features.

Finally, beyond the specific ‘best’ cases of Figs. 6A-C, we studied the performance in discriminating young from elderly subjects at the level of whole ensembles of predictor quadruplets. For every possible predictor quadruplet, we computed: the *precision* of discrimination, i.e. the fraction of correct classifications as old subjects; and the *sensitivity* of discrimination, i.e. the fraction of old subjects correctly inferred as such (see *Methods*). We then show in Fig. 6C the distributions of precision-sensitivity score pairs obtained for all the possible quadruplets. Among the different categories, quadruplets of SC_{ij} had the best median precision and quadruplets of $\text{MC}(ij)$ had the best median sensitivity. Quadruplets of mixed type features achieved on their turn both a median precision close to SC_{ij} quadruplets and a median sensitivity close to $\text{MC}(ij)$ quadruplets, confirming once again, at the ensemble level, that positive synergies between predictor types can be exploited to better extract age-related information.

Discussion

The structured intrinsic time-variability of rs FC may carry useful, generally disregarded information about ongoing neural dynamical processes and their age-related alterations. Here we characterized the coordinated evolution of rs FC, revealing correlations of FCD and MC with subject’s age and also with inter-subject variability in task performance.

Many studies in ‘chronnectomics’ have attempted isolating FC states that stereotypically reoccur across time and subjects (Hutchison et al., 2013b; Calhoun et al., 2014). However, the retrieved states and their number may be affected by the clustering algorithm used and by the availability of data. Furthermore, it may be difficult to statistically prove that FC is switching between states that are really distinct (Hindriks et al., 2016; Laumann et al., 2016). Here we bypassed FC state extraction, by focusing on sequential correlations in continuous and stochastic $\text{FC}(t)$ streams. We found that FCD trajectories ‘explore’ the space of FC configurations at a temporally inhomogeneous speed (Fig. 2D). Such anomalous random process may occur even within a single FC state, in such a way that the distance between FCD knots could become compatible with a scenario of overall FC stationarity (Hindriks et al., 2016).

Switching between FC knots and leaps may reflect the underlying complex dynamics of cortical circuits, with system’s trajectories alternatively exploring faster and slower manifolds in a complex system’s phase space (Jirsa et al., 2012; Hansen et al., 2015). From a functional perspective, walks of the Lévy type have been associated to optimal search, e.g., for food in an ecological environment (Viswanathan et al., 1999) or for winning bidding strategies in auctions (Radicchi et al., 2012). It is tempting to consider anomalous stochastic FCD as a neural process efficiently ‘foraging’ for cognitive resources by searching for FC patterns adapted to the information sharing and transfer demands (Battaglia et al., 2012; Kirst et al., 2016) of ongoing mental computations.

Theories of cognitive aging have advanced that a cause for declining performance would be the insufficient access to cognitive resources due to a reduced speed of information processing (Salthouse, 1996; Finkel et al., 2007). Cognitive aging has been associated to deficits in disengaging from active brain functional states, more than to alterations of the states themselves (Clapp et al., 2011; Cashdollar et al., 2013). In fact, aging affects FCD by reducing the reconfiguration speed of FC networks. Slowing down of cognition hence parallels slowing of FCD. Having said that, we do believe that more

and better-adapted experiments should be designed to probe speed of processing or task switching to move beyond mere conjectures. Speculatively, certain modifications of FCD may also be interpreted as a further example of the compensatory mechanisms ubiquitous in aging (Grady et al., 2012), e.g., the fact that elderly subjects' FCD leads to a more flexible FC modular structure, despite being slower (Fig. 3), even if the 'liquidity' of FC modules seems to anti-correlate rather than correlate with the MoCA score (Table 1).

Aging has a widespread impact on the strength of SC and FC (O'Sullivan et al., 2001; Salat, 2011; Andrews-Hanna et al., 2007; Ferreira & Busatto, 2013; Betzel et al., 2014) and also on the temporal variance $\sigma(\text{FC})$ of individual FC links (Grady & Garrett, 2014). However, age alterations of SC, FC, $\sigma(\text{FC})$, and MC are quite independent (Fig. S6) and yield non-redundant age information. As a result, mixing different categories of predictors can lead to superior precision and sensitivity in age prediction and age-group discrimination (Fig. 6). The combined tracking of SC-, FC- and MC-based features may thus lead to a superior parameterization of the "healthy" trajectory of aging and, potentially, to an earlier detection of deviations from it, providing new imaging-based markers in pathological aging. It has indeed already been observed that some early modification of rs FC in Alzheimer's disease can be explained as alterations of relative dwelling times, rather than alteration of the rs networks themselves (Jones et al., 2012).

The age dependency of FCD may be the expression of artifacts, such as modifications of the neurovascular coupling itself (D'Esposito et al., 2003) or other physiological processes of non-neural origin, such as breathing (Birn et al., 2006). Furthermore, stronger age-related effects on BOLD FCD are observed for short temporal windows – cf. analogous conclusions by Schlesinger et al. (2016) –, which are 'borderline' for the time resolution of fMRI and more sensitive to artifacts. Although windows of ~30s as the one we adopt in most of our analyses still provide an acceptable compromise between avoidance of artefacts and tracking of fast temporal FC fluctuations (Leonardi & Van De Ville, 2015), future studies will have to simultaneously look at FCD based on signals that reflect neural activations more directly and have a better time resolution, such as EEG (Chang et al., 2013). Our findings of correlations between FCD and cognitive performance (Fig. 5 and Table 1) also suggest, ultimately, that FCD changes are not artifactual and add to previous independent studies (Bassett et al., 2011; Shine et al., 2016) hinting at an actual link between rs BOLD FCD at a fast temporal resolution and task-relevant neural information processing.

Mean-field whole-brain computational models (Deco et al., 2011) provide finally a further welcome avenue for assessing the non-artifactual nature of FCD – virtual brains do not have blood –, while allowing, more importantly, for reverse-engineering its dynamic underpinnings. Generic whole-brain models are already able to qualitatively reproduce switching FCD (Hansen et al., 2015), but future simulations might be fitted to individual subjects via automated pipelines (Schirner et al., 2015) to render the FCD trajectory of evolution across aging in a more quantitative manner. Models embedding SC typical of different age classes may reproduce the slowing down of FCD as an emergent byproduct of SC 'disconnection' itself. Or, more likely, they may show that this disconnection must be compensated to account for observations by a drift of the global 'dynamic working point' of operation of cortical networks, which could be possibly induced by altered neuromodulation (Bäckman et al., 2006) or metabolism (Arenaza-Urquijo et al., 2013).

Author contributions

DB and VJ conceived the novel analytic methods; DB, TB and EH performed imaging data analysis; AD provided expertise and toolbox for DFA and model selection; PR supervised imaging experiments; PR, AD and SC conceived the cognitive and motor experiments; SC performed the cognitive and motor experiments and processed behavioral data; RM and JZ contributed to data pre-processing; DB, TB, EH, SC, AD, RM, JZ, PR and VJ wrote the paper.

Acknowledgments

This research was supported by the Brain Network Recovery Group (through the James S. McDonnell Foundation) and by EU funding (FP7-ICT BrainScales and Human Brain Project, grant no. 60402). DB was supported by the EU Marie Curie fellowship FP7-IEF 330792 (DynViB) and by the CNRS action InFinITI – ‘BrainTime’. We thank: Rodrigo Sigala, Sebastian Haufe, Michael Schirner, Simon Rothmeier for help in data acquisition; and Dionysios Perdikis, Rita Sleimen-Malkoun and Stephan Eule for discussions.

References

- Allen, E.A., Damaraju, E., Plis, S.M., Erhardt, E.B., Eichele, T., Calhoun, V.D., 2012. Tracking Whole-Brain Connectivity Dynamics in the Resting State. *Cerebral Cortex*. doi:10.1093/cercor/bhs352
- Andrews-Hanna, J.R., Snyder, A.Z., Vincent, J.L., Lustig, C., Head, D., Raichle, M.E., Buckner, R.L., 2007. Disruption of large-scale brain systems in advanced aging. *Neuron* 56, 924–935.
- Arenaza-Urquijo, E.M., Landeau, B., La Joie, R., Mevel, K., Mézenge, F., Perrotin, A., Desgranges, B., Bartrés-Faz, D., Eustache, F., Chételat, G., 2013. Relationships between years of education and gray matter volume, metabolism and functional connectivity in healthy elders. *NeuroImage* 83, 450–457.
- Bäckman, L., Nyberg, L., Lindenberger, U., Li, S.-C., Farde, L., 2006. The correlative triad among aging, dopamine, and cognition: current status and future prospects. *Neurosci Biobehav Rev* 30, 791–807.
- Bassett, D.S., Wymbs, N.F., Porter, M.A., Mucha, P.J., Carlson, J.M., Grafton, S.T., 2011. Dynamic reconfiguration of human brain networks during learning. *Proc Natl Acad Sci USA* 108, 7641–7646.
- Battaglia, D., Witt, A., Wolf, F., Geisel, T., 2012. Dynamic Effective Connectivity of Inter-Areal Brain Circuits. *PLoS Comp Biol* 8, e1002438.
- Betzel, R.F., Byrge, L., He, Y., Goñi, J., Zuo, X.-N., Sporns, O., 2014. Changes in structural and functional connectivity among resting-state networks across the human lifespan. *NeuroImage* 102P2, 345–357.
- Birn, R.M., Diamond, J.B., Smith, M.A., Bandettini, P.A., 2006. Separating respiratory-variation-related fluctuations from neuronal-activity-related fluctuations in fMRI. *NeuroImage* 31, 1536–1548.
- Buckner, R.L., 2004. Memory and executive function in aging and AD: multiple factors that cause decline and reserve factors that compensate. *Neuron* 44, 195–208.

- Calhoun, V.D., Miller, R., Pearlson, G., Adali, T., 2014. The Chronnectome: Time-Varying Connectivity Networks as the Next Frontier in fMRI Data Discovery. *Neuron* 84, 262–274.
- Cashdollar, N., Fukuda, K., Bocklage, A., Aurtentetxe, S., Vogel, E.K., Gazzaley, A., 2013. Prolonged disengagement from attentional capture in normal aging. *Psychol Aging* 28, 77–86.
- Castel, A.D., Craik, F.I.M., 2003. The effects of aging and divided attention on memory for item and associative information. *Psychol Aging* 18, 873–885.
- Chang, C., Liu, Z., Chen, M.C., Liu, X., Duyn, J.H., 2013. EEG correlates of time-varying BOLD functional connectivity. *NeuroImage* 72, 227–236.
- Chen, J.E., Chang, C., Greicius, M.D., Glover, G.H., 2015. Introducing co-activation pattern metrics to quantify spontaneous brain network dynamics. *NeuroImage* 111, 476–488.
- Clapp, W.C., Rubens, M.T., Sabharwal, J., Gazzaley, A., 2011. Deficit in switching between functional brain networks underlies the impact of multitasking on working memory in older adults. *Proc Natl Acad Sci USA* 108, 7212–7217.
- Daffertshofer, A., Peper, C.E., Frank, T.D., Beek, P.J., 2000. Spatio-temporal patterns of encephalographic signals during polyrhythmic tapping. *J Human Movement Science* 19, 475–498.
- Damaraju, E., Allen, E.A., Belger, A., Ford, J.M., McEwen, S., Mathalon, D.H., Mueller, B.A., Pearlson, G.D., Potkin, S.G., Preda, A., Turner, J.A., Vaidya, J.G., van Erp, T.G., Calhoun, V.D., 2014. Dynamic functional connectivity analysis reveals transient states of dysconnectivity in schizophrenia. *Neuroimage Clin* 5, 298–308.
- Damoiseaux, J.S., Rombouts, S.A.R.B., Barkhof, F., Scheltens, P., Stam, C.J., Smith, S.M., Beckmann, C.F., 2006. Consistent resting-state networks across healthy subjects. *Proc Natl Acad Sci USA* 103, 13848–13853.
- Davison, E.N., Schlesinger, K.J., Bassett, D.S., Lynall, M.-E., Miller, M.B., Grafton, S.T., Carlson, J.M., 2015. Brain Network Adaptability across Task States. *PLoS Comp Biol* 11, e1004029.
- Deco, G., Jirsa, V.K., McIntosh, A.R., 2011. Emerging concepts for the dynamical organization of resting-state activity in the brain. *Nat Rev Neurosci* 12, 43–56.
- Desikan, R.S., Ségonne, F., Fischl, B., Quinn, B.T., Dickerson, B.C., Blacker, D., Buckner, R.L., Dale, A.M., Maguire, R.P., Hyman, B.T., Albert, M.S., Killiany, R.J., 2006. An automated labeling system for subdividing the human cerebral cortex on MRI scans into gyral based regions of interest. *NeuroImage* 31, 968–980.
- D’Esposito, M., Deouell, L.Y., Gazzaley, A., 2003. Alterations in the BOLD fMRI signal with ageing and disease: a challenge for neuroimaging. *Nat Rev Neurosci* 4, 863–872.
- Ferreira, L.K., Busatto, G.F., 2013. Resting-state functional connectivity in normal brain aging. *Neurosci Biobehav Rev* 37, 384–400.
- Finkel, D., Reynolds, C.A., McArdle, J.J., Pedersen, N.L., 2007. Age changes in processing speed as a leading indicator of cognitive aging. *Psychol Aging* 22, 558–568.
- Geerligs, L., Renken, R.J., Saliasi, E., Maurits, N.M., Lorist, M.M., 2015. A Brain-Wide Study of Age-Related Changes in Functional Connectivity. *Cerebral Cortex* 25, 1987–1999.

- Gonzalez-Castillo, J., Hoy, C.W., Handwerker, D.A., Robinson, M.E., Buchanan, L.C., Saad, Z.S., Bandettini, P.A., 2015. Tracking ongoing cognition in individuals using brief, whole-brain functional connectivity patterns. *Proc Natl Acad Sci USA* 112, 8762–8767.
- Grady, C., 2012. The cognitive neuroscience of ageing. *Nat Rev Neurosci* 13, 491–505. doi:10.1038/nrn3256
- Grady, C.L., Garrett, D.D., 2014. Understanding variability in the BOLD signal and why it matters for aging. *Brain Imaging Behav* 8, 274–283.
- Hansen, E.C.A., Battaglia, D., Spiegler, A., Deco, G., Jirsa, V.K., 2015. Functional connectivity dynamics: modeling the switching behavior of the resting state. *NeuroImage* 105, 525–535.
- Hindriks, R., Adhikari, M.H., Murayama, Y., Ganzetti, M., Mantini, D., Logothetis, N.K., Deco, G., 2016. Can sliding-window correlations reveal dynamic functional connectivity in resting-state fMRI? *NeuroImage* 127, 242–256.
- Honey, C.J., Sporns, O., Cammoun, L., Gigandet, X., Thiran, J.P., Meuli, R., Hagmann, P., 2009. Predicting human resting-state functional connectivity from structural connectivity. *Proc Natl Acad Sci USA* 106, 2035–2040.
- Houweling, S., Daffertshofer, A., van Dijk, B.W., Beek, P.J., 2008. Neural changes induced by learning a challenging perceptual-motor task. *Neuroimage* 41, 1395–407.
- Hutchison, R.M., Womelsdorf, T., Gati, J.S., Everling, S., Menon, R.S., 2013a. Resting-state networks show dynamic functional connectivity in awake humans and anesthetized macaques. *Human Brain Mapping* 34, 2154–2177.
- Hutchison, R.M., Womelsdorf, T., Allen, E.A., Bandettini, P.A., Calhoun, V.D., Corbetta, M., Penna, Della, S., Duyn, J.H., Glover, G.H., Gonzalez-Castillo, J., Handwerker, D.A., Keilholz, S., Kiviniemi, V., Leopold, D.A., de Pasquale, F., Sporns, O., Walter, M., Chang, C., 2013b. Dynamic functional connectivity: promise, issues, and interpretations. *NeuroImage* 80, 360–378.
- Hutchison, R.M., Morton, J.B., 2015. Tracking the Brain's Functional Coupling Dynamics over Development. *J Neurosci* 35, 6849–6859.
- Jirsa, V., Huys, R., Pillai, A., Perdikis, D., Woodman, M. (2012) Connectivity and dynamics of information processing. In: *Principles of Brain Dynamics: Global state interactions*, Rabinovich, M.I., Friston, K.J. and Varona, P. eds. (The MIT Press).
- Jones, D.T., Vemuri, P., Murphy, M.C., Gunter, J.L., Senjem, M.L., Machulda, M.M., Przybelski, S.A., Gregg, B.E., Kantarci, K., Knopman, D.S., Boeve, B.F., Petersen, R.C., Jack, C.R., 2012. Non-stationarity in the “resting brain's” modular architecture. *PLoS ONE* 7, e39731.
- Kirst, C., Timme, M., Battaglia, D., 2016. Dynamic information routing in complex networks. *Nat Comms* 7, 11061. doi:10.1038/ncomms11061
- Laumann, T.O., Snyder, A.Z., Mitra, A., Gordon, E.M., Gratton, C., Adeyemo, B., Gilmore, A.W., Nelson, S.M., Berg, J.J., Greene, D.J., McCarthy, J.E., Tagliazucchi, E., Laufs, H., Schlaggar, B.L., Dosenbach, N.U.F., Petersen, S.E., 2016. On the Stability of BOLD fMRI Correlations. *Cerebral Cortex*. doi:10.1093/cercor/bhw265
- Leonardi, N., Van De Ville, D., 2015. On spurious and real fluctuations of dynamic functional connectivity during rest. *NeuroImage* 104, 430–436.

- Lindenberger, U., Oertzen, von, T., 2006. Variability in cognitive aging: From taxonomy to theory. In: Lifespan cognition: Mechanisms of change, Bialystok E and Craik FIM eds. (Oxford University Press), pp. 297-314.
- Liu, X., Duyn, J.H., 2013. Time-varying functional network information extracted from brief instances of spontaneous brain activity. *Proc Natl Acad Sci USA* 110, 4392–4397.
- Mandelbrot, B.B., 1983. *The Fractal Geometry of Nature* (Macmillan).
- Metzler, R., Jeon, J.-H., Cherstvy, A.G., Barkai, E., 2014. Anomalous diffusion models and their properties: non-stationarity, non-ergodicity, and ageing at the centenary of single particle tracking. *Phys. Chem. Chem. Phys.* 16, 24128–24164.
- Nasreddine, Z.S. et al., 2005. The Montreal Cognitive Assessment, MoCA: A Brief Screening Tool For Mild Cognitive Impairment. *J Am Geriatr Soc* 53, 695–699.
- O'Sullivan, M., Summers, P.E., Jones, D.K., Jarosz, J.M., Williams, S.C., Markus, H.S., 2001. Evidence for cortical "disconnection" as a mechanism of age-related cognitive decline. *Neurology* 57, 632–638.
- Radicchi, F., Baronchelli, A., Amaral, L.A.N., 2012. Rationality, irrationality and escalating behavior in lowest unique bid auctions. *PLoS ONE* 7, e29910.
- Salat, D.H., 2011. The declining infrastructure of the aging brain. *Brain Connectivity* 1, 279–293.
- Salthouse, T.A., 1996. The processing-speed theory of adult age differences in cognition. *Psychol Rev* 103, 403–428.
- Schirner, M., Rothmeier, S., Jirsa, V.K., McIntosh, A.R., Ritter, P., 2015. An automated pipeline for constructing personalized virtual brains from multimodal neuroimaging data. *NeuroImage* 117, 343–357.
- Schlesinger, K.J., Turner, B.O., Lopez, B.A., Miller, M.B., Carlson, J.M., 2016. Age-dependent Changes in Task-based Modular Organization of the Human Brain. *NeuroImage*. doi:10.1016/j.neuroimage.2016.09.001
- Shine, J.M., Bissett, P.G., Bell, P.T., Koyejo, O., Balsters, J.H., Gorgolewski, K.J., Moodie, C.A., Poldrack, R.A., 2016. The Dynamics of Functional Brain Networks: Integrated Network States during Cognitive Task Performance. *Neuron* 92, 544–554.
- Tagliazucchi, E., Wegner, von, F., Morzelewski, A., Brodbeck, V., Laufs, H., 2012. Dynamic BOLD functional connectivity in humans and its electrophysiological correlates. *Front Hum Neurosci* 6, 339.
- Ton, R., Daffertshofer, A., 2016. Model selection for identifying power-law scaling. *NeuroImage* 136, 215–226.
- Viswanathan, G.M., Buldyrev, S.V., Havlin, S., da Luz, M.G., Raposo, E.P., Stanley, H.E., 1999. Optimizing the success of random searches. *Nature* 401, 911–914.
- Yaesoubi, M., Miller, R.L., Calhoun, V.D., 2015. Mutually temporally independent connectivity patterns: a new framework to study the dynamics of brain connectivity at rest with application to explain group difference based on gender. *NeuroImage* 107, 85–94.
- Zimmermann, J., Ritter, P., Shen, K., Rothmeier, S., Schirner, M., McIntosh, A.R., 2016. Structural architecture supports functional organization in the human aging brain at a regionwise and network level. *Human Brain Mapping*. doi:10.1002/hbm.23200

Figures

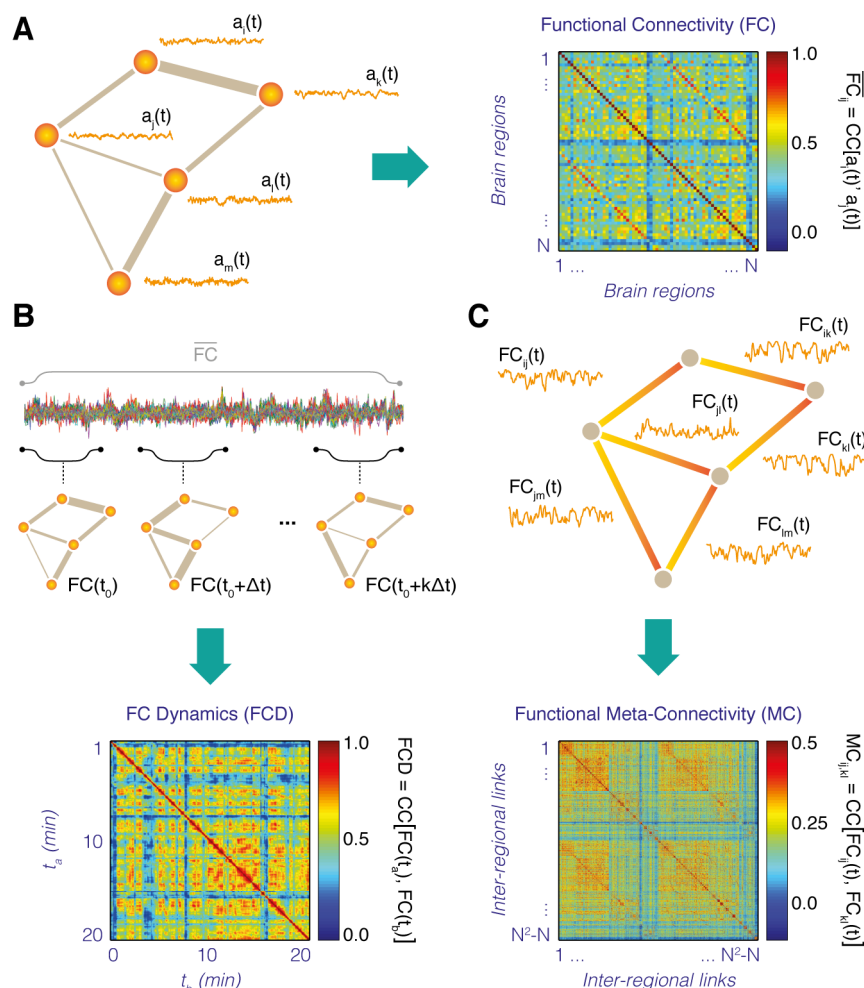


Fig. 1. From Functional Connectivity to Functional Connectivity Dynamics. (A) Traditionally, correlations between the BOLD activity time-series $a_i(t)$ of N different brain region nodes i and j (left) are averaged over long times and compiled into the entries FC_{ij} of a ‘static’ N -times- N Functional Connectivity (FC) matrix (right). (B) Sliding windows of a shorter temporal duration, it is possible to estimate a stream of time-resolved $FC(t)$ networks (top). The degree of similarity (inter-matrix correlation) between $FC(t)$ networks observed at different times is then represented into a T -times- T recurrence matrix, or *Functional Connectivity Dynamics* (FCD) matrix, where T is the total number of probed windows, depending on window size and overlap (bottom). (C) Alternatively, one can consider each individual FC link as a dynamic variable $FC_{ij}(t)$ attached to the graph edge between two regions i and j (top). Generalizing the construction of the FC matrix in panel (A), we can thus extract a $N(N-1)$ -times- $N(N-1)$ matrix of covariance between the time-courses of different $FC_{ij}(t)$ links. We re-baptized this inter-link covariance matrix as *Functional Meta-Connectivity* (MC) matrix.

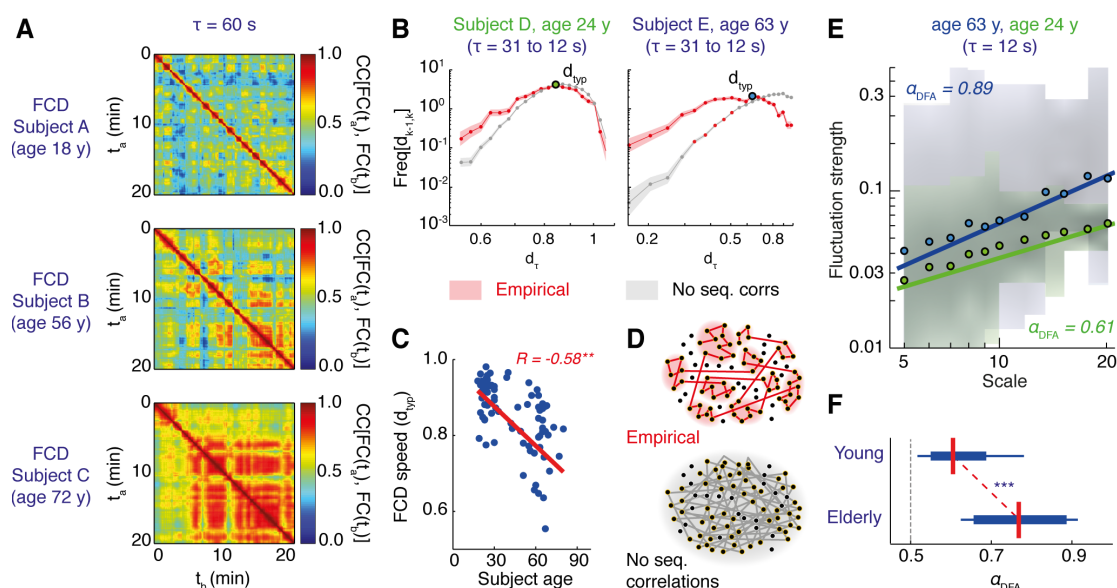


Fig. 2. Age effects on Functional Connectivity Dynamics. Correlations between FC networks observed at different times t_1 and t_2 during resting state are compiled into FCD matrices (cf. Figure 1B). (A) FCD matrices for subjects of increasing age (window size $\tau = 60$ s, see Fig. S2 for other τ -s). Blocks of large inter-network correlation indicate epochs in which FC is stable (*FCD knots*), separated by transients of faster FC reconfiguration (*FCD leaps*). Visual inspection suggested that FCD knots lasted longer with increasing age. This is confirmed by computing the rates of FC reconfiguration d_τ , or *FCD speed*. (B) Distributions of FCD speed, shown here for two representative subjects (log-log scale, pooled window sizes $12 \text{ s} \leq \tau < 31 \text{ s}$) displayed a peak at a value d_{yp} (*typical FCD speed*) and a fat left tail, reflecting an increased probability with respect to chance level to observe short FCD steps (95% confidence intervals are shaded: red, empirical; gray, chance level). (C) The FCD speed d_{yp} decreased with age (see Fig. S3 for larger τ -s). The FC space was seemingly explored through an anomalous random process in which short steps were followed by short steps with large probability (sequential correlations), leading to clustered trajectories (panel D, top). This contrasts with a standard random process, visiting precisely the same FC configurations but without long-range correlations (panel D, bottom). (E-F) The persistence of FCD could be proved through a Detrended Fluctuation Analysis (DFA). (E) DFA log-log plots for two representative subjects ($\tau = 12$ s, see Fig. S4 for DFA at other τ -s). Shadings correspond to the inter-quartile range for the probability densities of the fluctuation strength at different scales of observation, estimated prior to maximum-likelihood fitting (plotted dots give the mean values). DFA exponents α_{DFA} are generally larger than 0.5, indicating anomalously persistent fluctuations, and are larger for elderly than for young subjects (panel F, two groups: $N = 26$, 18-25y; and 57-80y, $N = 33$; $p < 0.001$, U Mann Whitney).

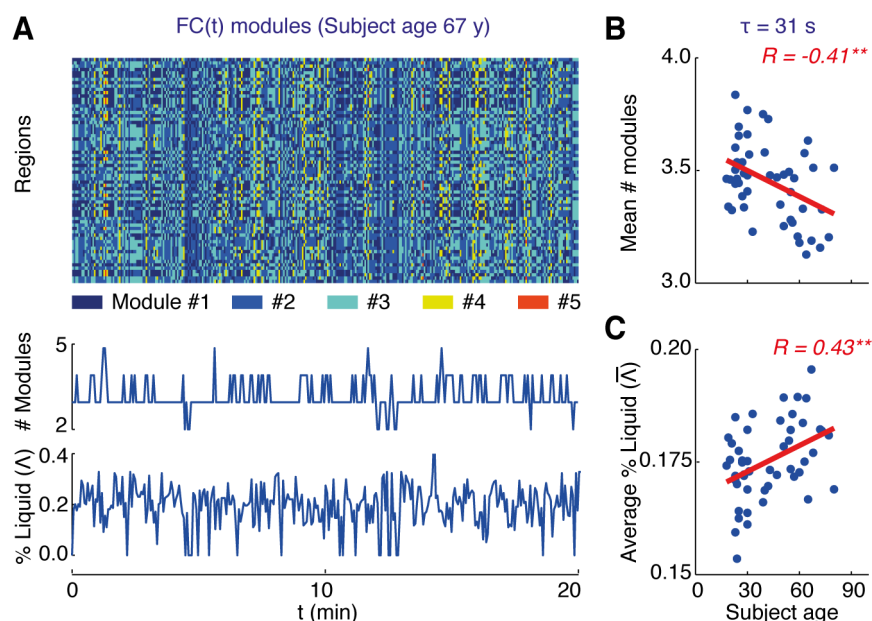


Fig. 3. Age effects on the temporal stability of the FC modular structure. We studied how the community structure of $FC(t)$ networks across time as an effect of ongoing rs FCD, adopting a window size of $\tau = 31$ s (16 TR, window step of 1 TR). We then re-clustered the obtained network modules across the different time-slices to maximize their consistency between consecutive windows. (A) Membership of different brain regions to different $FC(t)$ modules for a representative subject (top). The figure also shows the corresponding time-courses for the number of retrieved FC network modules (middle) and for the ‘liquid fraction’ $\Lambda(t)$, i.e. the fraction of brain regions transiting from one module to another across one time step and the next (bottom). (B) The average number of retrieved $FC(t)$ modules decreased with age ($p < 0.01$, bootstrap with replacement); (C) The time-averaged liquid fraction $\bar{\Lambda}$ within each module increased with age ($p < 0.01$, bootstrap with replacement), denoting a reduced temporal stability of the $FC(t)$ modular structure, despite the overall slower speed of FCD.

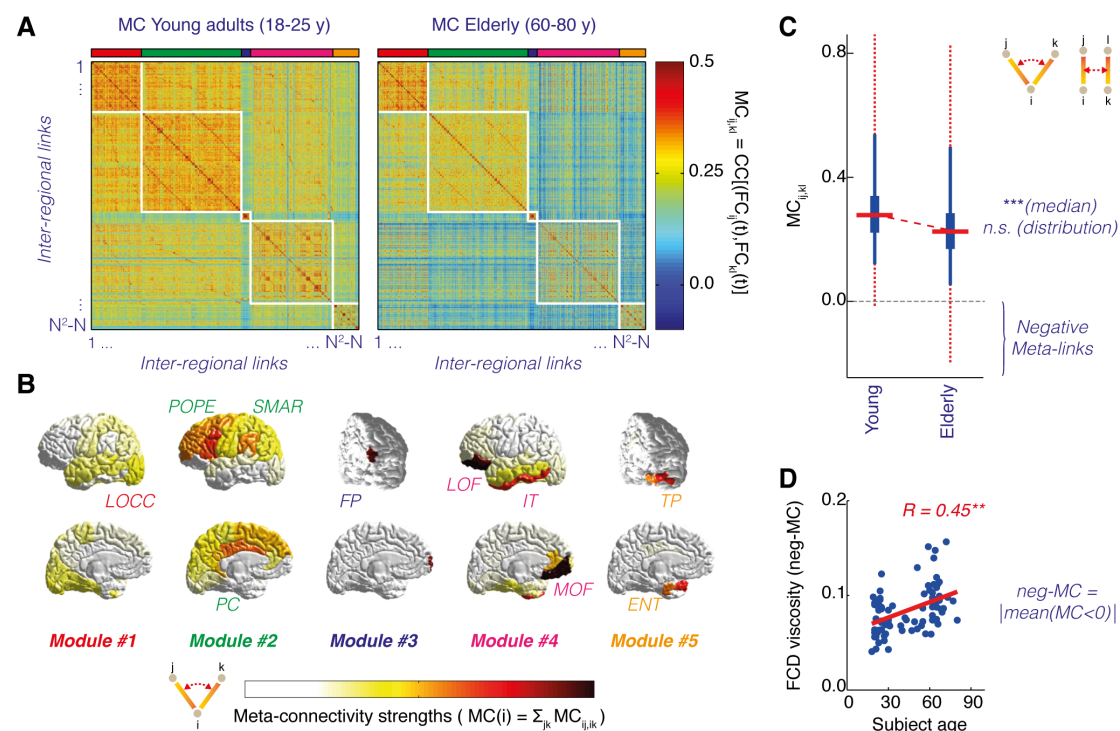


Fig. 4. Age effects on inter-link Meta-Connectivity. Correlations between the time-courses of pairs of inter-regional FC links are compiled into *Meta-Connectivity* (MC) matrices (cf. Figure 1C). (A) Group-averaged MC for two distinct age groups ($N = 28$, 18-25y; and 57-80y, $N = 34$) based on a FCD window size of $\tau = 31$ s (16 TR, window step of 1 TR, as in Fig. 3). In panel (B) regions are colored according to their meta-connectivity weight $MC(i)$, i.e. the sum of the strengths of meta-links between FC links incident on the i -th region (average over the two hemispheres). Modules of temporally co-varying links were organized around distinct meta-hub regions with elevated MC weight. (C) Distributions of MC strengths for the two age groups (all trimer $MC_{ij,kl}$ and tetramer $MC_{ij,kl}$ meta-links, cf. upper right cartoon diagrams). Boxes display the interquartile range, whiskers the 95% confidence interval and dotted-red lines the full range, revealing outliers. Median strengths were different between age groups ($p < 0.001$, Kruskal-Wallis) but not the distributions themselves. However, negative outlier meta-links developed with age. (D) At the single subject level, *neg-MC*, i.e. the total sum of the absolute values of negative MC entries, correlates with age ($p < 0.01$, bootstrap). In other words, the FCD flux becomes more ‘viscous’, with a frustrated freedom of fluctuation, due to conflicting positive and negative influences.

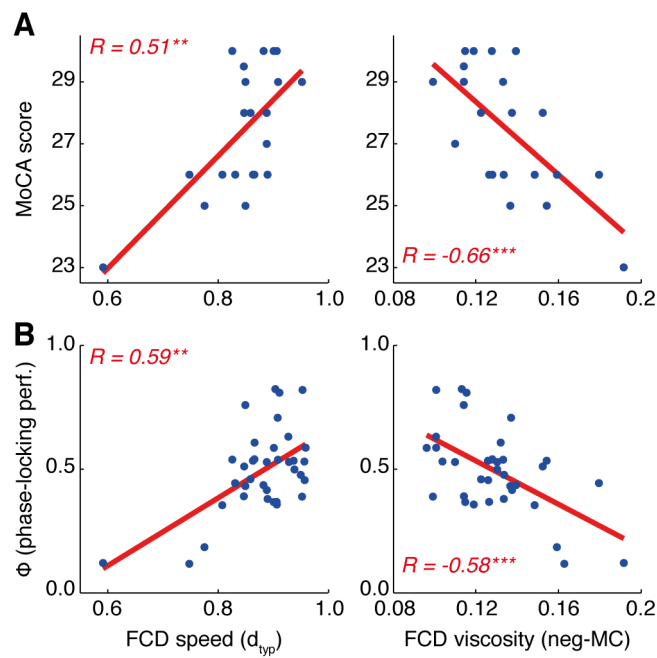


Fig. 5. Correlation between FCD and cognitive/visuo-motor performance. Cognitive performance was tested via Montreal Cognitive Assessment (MoCA, $N = 21$) and visuo-motor performance in a unimanual visuo-motor task ($N = 36$), in which hand pressure on a rubber balloon had to be frequency-locked with the speed rotation of a visual stimulus during the fMRI scan. Typical FCD speed d_{typ} (left) and FCD viscosity neg-MC (right) correlated or anti-correlated, respectively, with both (A) the global MoCA score, and (B) the average frequency-locking coefficient Φ ($**p < 0.01$; $***p < 0.001$; bootstrap). Partial correlations in which the common declining trend with age was regressed out were also significant (see Table 1).

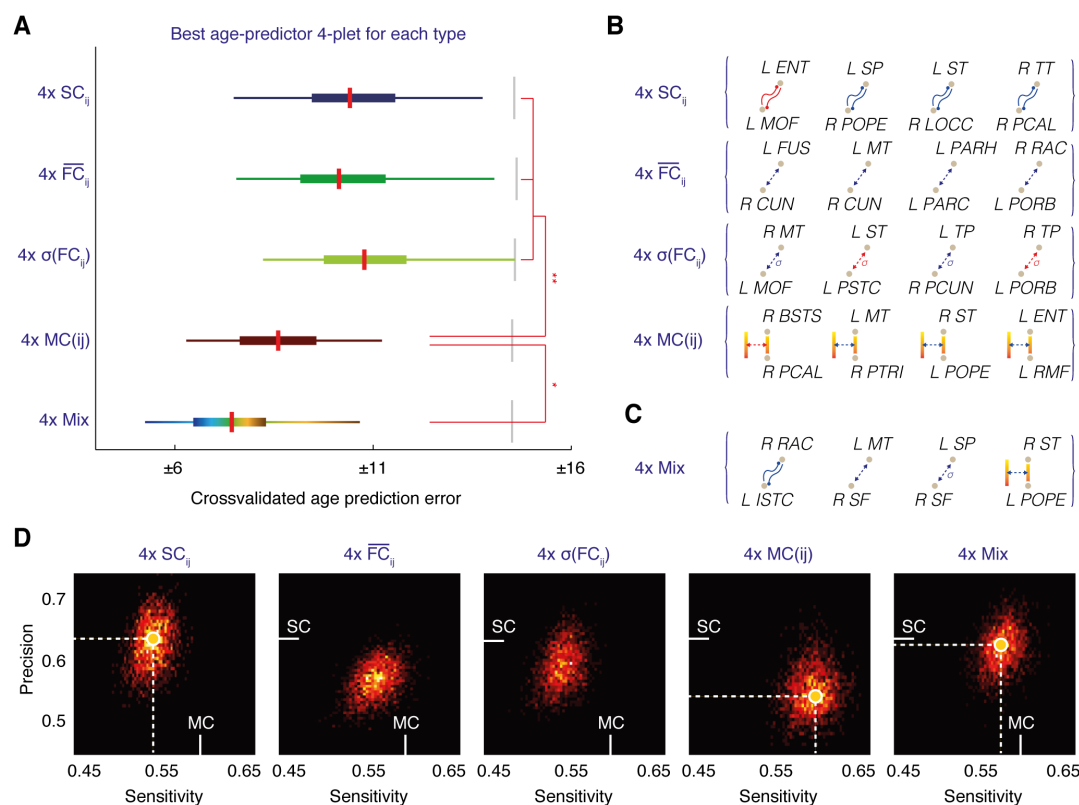


Fig. 6. FCD brings complementary information about brain aging. To gauge the relative amount of age-related information conveyed by different types of predictive features, we performed age-prediction based on a simple linear regression scheme between age and different quadruplets of features. Panel A shows boxplots (whiskers, 95% c.i.; box, interquartile range; red line, median) of the absolute cross-validated prediction error based on the best quadruplet of homogeneous-type features (4x) chosen among: strengths SC_{ij} of SC links; strengths \overline{FC}_{ij} of time-averaged FC links; variances over time $\sigma(FC_{ij})$ of FC links; and, meta-connectivity strengths $MC(ij) = \sum_{kl} MC_{ij,kl}$. We also considered mixed quadruplets including one feature for each of the four feature categories. Quadruplets of $MC(ij)$ features achieved the smaller median cross-validated prediction error, further improved by quadruplets with mixed feature types (respectively, $p < 0.01$ and $p < 0.05$, Bonferroni-corrected, Kruskal-Wallis). Panels B-C show the best quadruplets of same-type features (B) or the best mixed-type quadruplet (C), corresponding to the prediction performances shown in panel A. Icons with red (blue) links correspond respectively to predicting features correlating (anti-correlating) with age. (E) When discriminating subjects into two classes (older or younger than the median age), quadruplets of different types reached different precision and sensitivity in classification. We display joint distributions (over all the possible quadruplets for each given type) of the achieved precision and sensitivity scores (cross-validated median). While SC-type quadruplets were the most precise, MC-type quadruplets were the most sensitive. Mixed-type quadruplets achieved high precision (SC-like) and high sensitivity (MC-like) simultaneously, profiting of a positive synergy between the complementary information conveyed by different predictors.

Tables

Table 1. Significant correlations between FCD markers and cognitive/visuo-motor performance

Type of correlation	Median	Bootstrap 95% c.i.
CC(neg-MC, MoCA)	0.66	(0.40, 0.82)***
CC(neg-MC, MoCA Age)	0.59	(0.35, 0.75)***
CC(neg-MC, Φ)	0.58	(0.33, 0.74)***
CC(neg-MC, Φ Age)	0.50	(0.17, 0.70)**
CC($d_{\eta p}$, MoCA)	0.51	(0.21, 0.72)**
CC($d_{\eta p}$, MoCA Age)	0.41	(0.05, 0.68)*
CC($d_{\eta p}$, Φ)	0.59	(0.10, 0.78)**
CC($\bar{\Delta}$, MoCA)	-0.32	(-0.49, -0.02)*

We report 95% bootstrap confidence intervals for all significant correlations between FCD metrics and performance scores. Stars indicate the confidence level up to which the reported correlation was tested as significant: * $p < 0.05$; ** $p < 0.01$; *** $p < 0.001$ (bootstrap with replacement).

Methods

Contact for reagent and resource sharing

Further information and requests for resources should be directed to and will be fulfilled by the Lead Contact, Demian Battaglia (demian.battaglia@univ-amu.fr).

Experimental model and subject details

Subjects. Overall $N = 85$ healthy adult subjects ($N = 53$ females, $N = 32$ males) were voluntarily recruited at Charité - Universitätsmedizin Berlin to participate in rs fMRI and DSI scans and, for a subset of them, also in a visuo-motor study. The first subset of $N = 49$ subjects ('rs-only') had ages uniformly distributed over the 18-80y range. The second set of $N = 36$ subjects ('rs+tasks') was further split into a first ($N = 15$, 20-25 yrs) and a second ($N = 21$, 59-70 yrs) age groups. All subjects had no self-reported neurological, psychiatric or somatic conditions. For the 'rs+tasks' subset, healthy cognitive function was furthermore assessed with the Montreal Cognitive Assessment (MoCA) (Nasreddine et al., 2005). For all the analyses of Figs. 1-4 and S1-6, in which cognitive performance was not relevant, we merged the two subsets of subjects. We distinguished for inter-group comparisons between a '*Young group*' composed of subjects in the first age-quartile of the 'rs-only' subset and the first age group of the 'rs+tasks' subset (overall $N = 28$, 18-25 yrs, median age = 22.5 yrs), and an '*Elderly group*' composed of subjects in the fourth age-quartile of the 'rs-only' subset and the second age group of the 'rs+tasks' subset (overall $N = 33$, 59-80 yrs, median age = 65 yrs).

In addition to general exclusion criteria for participation in an MRI experiment, subjects with a self-reported musical background were excluded, as musical training may affect the performance of the rhythmic visuo-motor task. Left-handed subjects, identified using the Edinburgh Handedness Inventory, were also excluded. Subjects were informed of the procedure of the study and basics of fMRI acquisition, and written consent was obtained prior to data collection. The study was performed in accordance with the local medical ethics committee protocol at the Charité Hospital (Berlin, Germany).

Method details

MRI acquisition. Magnetic resonance imaging (MRI) acquisition was performed on a 3T Siemens Trim Trio scanner. Every subject was scanned in a session which included a localizer sequence (3, 8mm slices, repetition time [TR] = 20 ms, echo time [TE] = 5 ms, voxel size = $1.9 \times 1.5 \times 8.0$ mm, flip angle [FA] = 40° , field of view [FoV] = 280 mm, 192 mm matrix), a T1-weighted high-resolution image (4:36 minutes, MPRAGE sequence, 192, 1mm sagittal slices, voxel size $1 \times 1 \times 1$ mm, TR = 1940 ms, TE = 2.52 ms, FA = 9° , FoV = 256 mm, 256 mm matrix), a T2 weighted image (2:16 minutes, 48, 3mm slices, voxel size $0.9 \times 0.9 \times 3$ mm, TR = 2640 ms, TE1 = 11 ms, TE2 = 89 ms, FoV 220 mm, 256 mm matrix), followed by diffusion weighted imaging (8:23 minutes, 61, 2mm transversal slices, voxel size = $2.3 \times 2.3 \times 2.3$ mm, TR = 7500, TE = 86 ms, FoV 220 mm, 96 mm matrix). Subjects were then removed from the scanner to have their EEG cap put on, and then simultaneous fMRI-EEG images were acquired in a single run (22:30 minutes, BOLD T2*-weighted, 32, 3mm transversal slices, voxel size = $3 \times 3 \times 3$ mm, TR = 1940

ms, TE = 30ms, FA = 78°, FoV = 192 mm, 64 mm matrix). Five dummy scans were automatically discarded by the Siemens scanner.

fMRI data preprocessing. fMRI data was preprocessed following Schirner et al. (2015). Here, FEAT (fMRI Expert Analysis Tool) first-level analysis from the FMRIB (Functional MRI of the brain) software was used. Motion correction was performed using EPI field-map distortion correction, BET brain extraction, and high-pass filtering (100s) to correct for baseline signal drift, MCFLIRT to correct for head movement across the trial. We checked that additional head movement correction by regressing out the six FSL head motion parameters did not significantly modify correlations with age of FCD and MC markers extracted from our BOLD time series. Functional data was registered to individual high-resolution T1-weighted images using linear FLIRT, followed by nonlinear FNIRT registration to Montreal Neurological Institute MNI152 standard space. Voxel-level BOLD time series were reduced to 68 different brain region-averaged time series, according to a Desikan parcellation (Desikan et al., 2006). See table S1 for the regions under consideration. We did not perform slice-timing correction, smoothing, or normalization of BOLD intensities to a mean.

Resting state. During resting state scans, subjects were to remain awake and reduce head movement. Head cushions were used to minimize head movement, and earplugs were provided. Scans for the ‘rs-only’ and the ‘rs+task’ subsets of subjects had different durations. For the ‘rs-only’ subset, 20m of uninterrupted rs scan were performed. For the ‘rs+task’ subset, five minutes of rs were collected before the task acquisition (see later), and then further five minutes after the task.

Visuo-motor coordination task (frequency-locking Φ score). The $N = 36$ subjects in the ‘rs+tasks’ subset also succeeded in performing a visuo-motor coordination task while in the scanner. The task followed a unimanual paradigm, which was adapted from a bimanual paradigm introduced in (Houweling et al., 2008). During the task, subjects were told to lay still inside the scanner with an air-filled rubber ball in their right hand. A screen, animated using a custom-made LabView program, was projected in the scanner. To reduce eye movement, subjects were instructed to fix their gaze at a cross, displayed in the middle of the screen between two rotating disks. The left disk served as visual cue, rotating at a computer-generated speed, while the subject’s squeezing of the ball controlled the speed of the right disk. The goal was to make the subject-generated rotating disk align (counter) rotation with the computer-generated rotating disk, which was done by squeezing the rubber ball in a 4:3 frequency to the visual cue. For perfect performance, the two disks would rotate in synchrony. Because the computer-generated disk rotated at a 4:3 frequency to the subject-generated circle, subjects had to squeeze the ball at 1.35 cycles per second to match the 1.8 cycles per second of the computer-generated disk in order to achieve synchrony.

Behavioural measures were collected (1 performance score per trial) based on the frequency locking of the two rotating circles. If the two disks rotated perfectly in-synchrony (i.e. subject was able to match the frequency of bulb-squeezing to the computer generated cue), the performance score would be 1. Not frequency-locked rotations of the two disks would result in a performance score of 0. More specifically, the frequency locking of the computer-generated circle and the subject-generated disk was quantified by the normalized spectral overlap between the power spectra of the two forces, P_x and P_y , as described in detail in (Daffertshofer et al., 2000):

$$\Phi = \frac{2 \int P_x(f) P_y(\rho f) df}{\int [P_x^2(f) + P_y^2(\rho f)] df}$$

with $q = 4/3$, corresponding to the target frequency ratio between the two rotating disks. Behavioural performance was expected to improve across trials as subjects learned the task, but in this study focused just on the average performance over the ten trials, ignoring learning.

MoCA cognitive assessment. MoCA assessment was performed by $N = 21$ elderly subjects of the ‘rs+tasks’ subset. The MoCA includes multiple sub-tasks probing different cognitive domains such as: short-term memory and delayed recall; visuo-spatial abilities; phonemic fluency, verbal abstraction and naming; sustained attention and concentration; working memory; executive control in task switching; spatio-temporal orientation. The test was administered in a German version (downloadable from <http://www.mocatest.org>). The maximum global score ‘MoCA’ achievable is of 30 points, up to 5 of which are contributed from the partial score ‘MoCA-wm’ from the working memory (‘Erinnerung’) task. Participants were considered in good/healthy mental state, when achieving scores higher than 25. All details can be found in (Nasreddine et al., 2005).

Quantification and statistical analysis

Extraction of time dependent Functional Connectivity. As, e.g., in (Allen et al., 2012), time-dependent Functional Connectivity matrices $FC(t)$ were estimated by sliding a temporal window of fixed duration τ and by evaluating zero-lag Pearson correlations between rs BOLD time series $a_i(t)$ from different brain regions:

$$FC_{ij}(t) = CC(a_i, a_j) |_{[t, t+\tau]} = \langle (a_i - \langle a_i \rangle) (a_j - \langle a_j \rangle) \rangle |_{[t, t+\tau]}$$

where temporal averages $\langle \cdot \rangle$ are taken over the restricted time interval $[t, t + \tau]$. All entries were retained in the matrix, independently of whether the correlation values were significant or not or without fixing any threshold (i.e., we treated FC_{ij} entries as descriptive *features* operationally defined by the above formula).

Evaluation of Functional Connectivity Dynamics (FCD) matrices. We introduced a notion of similarity between any two $FC(t_1)$ and $FC(t_2)$ matrices following (Hansen et al., 2015), based on the Pearson correlation between the entries of their upper-triangular parts:

$$FCD(t_a, t_b) = CC[\text{uppertri}(FC(t_a)), \text{uppertri}(FC(t_b))]$$

FCD matrices depend thus on the window-size τ adopted when extracting the $FC(t)$ stream.

Evaluation of FCD step lengths and their distribution. Correlation distance provide a natural (bounded) metric for the space of $FC(t)$ matrices. We can measure the distance traveled in FC space when stepping from one matrix $FC(t)$ to the next matrix in a sequence by evaluating:

$$d_\tau(t) = 1 - FCD(t, t + \tau)$$

Since the time step τ is maintained constant, these step lengths can be interpreted as rates of FC reconfiguration across time, and, thus, FCD speed.

It was difficult to estimate histograms of d_τ at the single subject level based on a single window-size τ because the number of sampled points within a single rs fMRI session was too small, especially for the longer window-sizes. Observing that the single-subject histograms that we obtained were similar for close window sizes, we chose to group observations obtained for different scales into three size-groups: ‘slow’ window-sizes (270s to 93s), ‘normal’ window-sizes (91s to 33s) and ‘fast’ window-sizes (31s to 12s).

The exact choice of included τ within each size-group was done to have τ homogeneously distributed over the size-group range and to have, after pooling, roughly the same number of d_τ observations available for building each of the three histograms (hence the larger ranges for the ‘slow’ and ‘normal’ size-groups, since the longer the τ the fewer non-overlapping windows could be allocated within the fixed length of the imaging session). Histograms for the three size-groups averaged over all subjects can be seen in Fig. S3A, together with a group-averaged histogram for ultra-fast window-sizes (10s to 6s), which still surprisingly has a ‘well-behaved’ shape. Single-subject histograms for the ‘fast’ size-group are shown in Fig. 2B. Confidence intervals for the histograms were evaluated according to a standard Agresti-Coull binomial proportion approximation.

The typical FCD speed d_{typ} was determined as the mode of a single-subject window-sizes pooled d_τ histogram and was as such dependent on the chosen size-group. When there were multiple d_τ values associated to the same maximum count then d_{typ} was given by the average of these multiple d_τ values.

Histograms under the null hypothesis of lack of sequential correlations were computed as above, apart from the following change. Before computing the d_τ values, the order of the observed FC(t) matrices in the observed stream was randomly permuted. In this way the FC mean and variance were preserved for each possible link, but the eventual sequential correlations were disrupted by construction. The randomization of order was performed 500 times and independently for each of the window sizes pooled to build the overall null hypothesis sample. With respect to null hypothesis expectations, single subject histograms very frequently showed: an under-representation of long step lengths; an over-representation of short step lengths; or both. We studied how frequent these two types of discordancies from chance-level expectations were by computing d_τ histogram made of 20 d_τ bins for all subjects and all window-sizes τ (no longer pooled). We ignored the actual values of the center of the twenty d_τ bins (which were different for each of the τ -s) and only considered their ordinal rank – always 1 to 20 for all τ -s –, in order to systematically compare across different window-sizes τ in which bins (relatively short or relatively long step lengths) an over-representation or an under-representation of counts were significantly occurring. The results of this analysis are shown in Fig. S3C.

Detrended Fluctuation Analysis (DFA). The Detrended fluctuation analysis (DFA) allows us detecting intrinsic statistical self-similarity embedded in a seemingly non-stationary time series. It is particularly adapted to the study of time series that display long-range persistence, and it is in this sense similar to other techniques, such as Hurst exponent analysis, requiring however the stationarity of the analyzed signal. See (Metzler et al., 2014) for a review. In order to capture self-similarity and auto-correlations among increments in a time series, DFA infers a self-similarity coefficient by comparing the detrended mean square fluctuations of the integrated signal over a range of observation scales in a log-log plot. If the log-log plot has an extended linear section, (i.e. if the scaling relation is a genuine power-law over a reasonably broad and continuous range of scales, see later for the meaning of ‘genuine’), it means that fluctuations ‘look the same’ across different temporal scales, i.e. we have statistically the same fluctuations if we scale the intensity of the signal respecting the DFA exponent.

We performed here DFA over the time series of d_τ ’s to detect sequential auto-correlations within them. First the sequence $d_\tau(t_1), d_\tau(t_2), \dots, d_\tau(t_L)$ was converted into an unbounded process:

$$D_{\tau}(t_i) = \sum_{\ell=1}^i d_{\tau}(t_{\ell})$$

Let K denote the number of samples in the time series, that are split into M non-overlapping segments $q = 1 \dots M$ of length k each, with $M = \lfloor K/k \rfloor$. For each segment q the fluctuation strength was computed as the squared difference between $D_{\tau}(t)$ and its trend $D_{\tau}^{(\text{trend})}(t)$ (in the linear case this is the regression line of $D_{\tau}(t)$ over the interval $t = 1 \dots k$):

$$F_q^2(k) = \frac{1}{k} \sum_{l=0}^{k-1} \left[D_{\tau}(t_{q+l}) - D_{\tau}^{(\text{trend})}(t_{q+l}) \right]^2$$

In the case of scale-free correlation this fluctuation strength scales with segment size k . That is, (on average) one finds a linear power law of the form:

$$\log\langle F_q(k) \rangle = \alpha_{\text{DFA}} \log k + C$$

The scaling parameter α_{DFA} is the primary outcome measure of DFA. In the case of the scale-free processes with the aforementioned power law, α_{DFA} resembles the Hurst exponent (Metzler et al., 2014), leading to the interpretation:

- . $0 < \alpha_{\text{DFA}} < 0.5$: d_{τ} – or D_{τ} – contains anti-persistent fluctuations
- . $\alpha_{\text{DFA}} = 0.5$: d_{τ} is uncorrelated white Gaussian noise – or D_{τ} resembles Brownian motion
- . $0.5 < \alpha_{\text{DFA}} < 1$: d_{τ} – or D_{τ} – contains persistent fluctuations
- . $1 \leq \alpha_{\text{DFA}}$: d_{τ} is non-stationary (strictly speaking, DFA is undefined in this case)

Prior to construing outcome values, however, it is mandatory to verify that a linear power law scaling actually exists. If it was not the case indeed the output value α_{DFA} could not be interpreted as a scaling exponent, but just as yet another meaningless number. Following (Ton & Daffertshofer, 2016), we tested the hypothesis of power-law scaling using a (Bayesian) model comparison approach. This allowed identifying the subjects for which the DFA log-log plot was better fit by a straight line than by any other tested alternative model. Only these subjects with a proper linear section in the DFA log-log plot were retained for the following steps of DFA exponent extraction and analysis of correlations with age.

In order to test the hypothesis of power law against alternative models, we evaluated the density of fluctuations over the consecutive segments, i.e. the density of $F_q(k)$ – beyond its mean value $\langle F_q(k) \rangle$ – using a kernel source density estimator. Based on this probability density, one can estimate the log-likelihood for a certain model to generate fluctuations of a given strength (on a log-scale) as a function of $\log k$. To perform model selection, the toolbox then computes the corrected Akaike Information criterion for each one of the tested models:

$$\text{AICc} = -2 \log \mathcal{L}_{\max} + 2p + \frac{2p(p+1)}{\mathcal{M} - p - 1}$$

where p is the number of free parameters to fit in the model and the number of points used to estimate the density of $F_q(k)$. Note that this model selection criterion automatically embeds a penalization for models with larger number of parameters, thus protecting against over-fitting. The model yielding the lowest AICc was selected as the

relatively best one, and in the case this was the linear one the corresponding \mathcal{L}_{max} -fitting parameter was considered as α_{DFA} .

To improve fitting and model selection we increased the number of available data-points by extracting more than just one d_t sequence from each given subject. Additional d_t sequences were constructed based on streams of stepped FCD windows with the same length τ , but with slightly shifted beginnings. In detail, in addition to the standard sequence $d_t(t_1), d_t(t_2), \dots, d_t(t_{L-1})$, we also extracted also a second sequence $d_t(t_1 + \delta t), d_t(t_2 + \delta t), \dots, d_t(t_{L-1} + \delta t)$, a third sequence $d_t(t_1 + 2\delta t), d_t(t_2 + 2\delta t), \dots, d_t(t_{L-1} + 2\delta t)$, ... and, finally, a last sequence $d_t(t_1 + q\delta t), d_t(t_2 + q\delta t), \dots, d_t(t_{L-1} + q\delta t)$ with $q\delta t < \tau$ and $(q+1)\delta t \geq \tau$. We subsequently performed independent DFAs for each one of these shifted sequences and merged the associated clouds of k vs $DFA(k)$ points prior to model selection.

We used a range of $5 < k < 20$, to discard data chunk sizes that were too short or long data chunk sizes yielding an overall number M of chunks that was too small.

Note that our DFA exponents still depend on the FCD window-size τ , which also provides the actual unit of measure for DFA scales. The k values of d_t 's included in each DFA chunk are evaluated based on $(k+1)\tau$ s of BOLD rs activity. Therefore, the robustness of DFA results must still be verified across different FCD window-sizes, as shown in Fig. S4. We based the analysis shown in Fig. 2E-F with a window-size of $\tau \sim 12$ s (and hence estimated the scaling exponent α_{DFA} over time-scales between 60 s and 240 s). In Fig. S4B the significance of age-to- α_{DFA} correlation at the single-subject level is shown also for different τ -s via permutation testing. The significance of inter-group differences between α_{DFA} values for different τ -s was assessed via the U-Mann Whitney non-parametric two-sided test (Fig. S4C). All tests were performed with different group sizes at every considered τ value, since different subjects could be considered or not to show a genuine power-law scaling for different τ -s.

A genuine power-law scaling in the DFA of subjects within the 'rs+task' subgroup could be established only for very few subjects and not always the same for different τ -s. This was probably due to the shorter length of rs BOLD time-series acquired for the 'rs+task' subset of subjects. Therefore, we limited DFA to the 'rs only' subset of subjects and correlations of α_{DFA} with cognitive and visuo-motor performance could not be tested.

FC modular flexibility analysis. To study how the modular structure of $FC(t)$ matrices changes across time as an effect of ongoing FCD, we performed a modular analysis of the graph structure of each $FC(t)$ matrix separately.

We used the Louvain algorithm to extract the modules of each of the networks $FC(t_a)$ separately. This involves an iterative scheme in which modules obtained at a given iteration step were used as the initial condition for the next step until when the obtained modularity goal function converged. The procedure was repeated 500 times and the module partition associated to the best score was maintained. We denote the obtained modules as $M_1(t_a), M_2(t_a), \dots, M_{K(a)}(t_a)$ where $K(a)$ is the number of FC modules extracted at time t_a . Since modules were generated independently for each considered time-window, there was no guarantee that a module $M_k(t_a)$ was related to a module $M_k(t_b)$ with which it – contingently – shared the same module index. For instance, it might be that the module at time $M_1(t_a)$ has a larger overlap with the module $M_4(t_b)$ than with the module $M_1(t_b)$. We therefore relabeled the module indices in order to guarantee the larger overall similarity across time between all modules sharing a common label. This

relabeling enabled us to meaningfully track the displacement of brain regions between different modules. To align the retrieved modules, we determined inter-module distance as the number of elements in the set-theoretical symmetric difference between them:

$$\text{dist}[M_i(t_a), M_j(t_b)] = \text{size}(M_i(t_a) \Delta M_j(t_b))$$

where:

$$A \Delta B = (A - B) \cup (B - A)$$

This was followed by a modified K -means clustering of the modules: i) choosing K , the maximum number of modules as the maximum $K(a)$ observed across time in the rs session for each given subject; ii) by using the above definition of inter-module distance as metric for the clustering; and, iii) by imposing that at each step of the K -means iterative algorithm (including the final one after convergence) every temporary cluster always included one and only one module deriving from each of the time-windows. After convergence of the clustering algorithm, all modules within each of the clusters of modules were reassigned a common label corresponding to the index of the K -means cluster. For instance, a given cluster of modules Q could contain modules $Q = \{M_4(t_1), M_2(t_2), M_5(t_3), \dots, M_3(t_{\max} - \delta t), M_1(t_{\max})\}$. All these modules were then relabeled as $\{M_Q(t_1), M_Q(t_2), M_Q(t_3), \dots, M_Q(t_{\max} - \delta t), M_Q(t_{\max})\}$ after our matching via re-clustering procedure. For the analyses underlying Fig. 3 we adopted $\delta t = 1.94$ s (corresponding to one TR). The module labels indicated in the top panel of Fig. 3A correspond to the labels Q after re-clustering of modules. The middle plot gives the evolution over time of $K(a)$ for a specific subject.

Next, we estimated the fractions of brain regions changing module when moving from a time t to the following time $t + \delta t$. The number of region-switching events affecting a given module Q was given by:

$$\lambda_Q(t) = \text{size}(M_Q(t) \Delta M_Q(t + \delta t))$$

We evaluated the time-dependent ‘liquid fraction’ of regions as the following quantity (averaged over the modules present at time t):

$$\Lambda(t) = \frac{1}{K(t)} \sum_Q \frac{\lambda_Q(t)}{\text{size } M_Q(t)}$$

For a specific subject this quantity is plotted in Fig. 3A’s bottom panel. Figs. 3B and 3C show correlations between subject age and the averages over time of the number of modules $K(t)$ and of the liquid fraction $\Lambda(t)$, respectively.

MC analysis. Out of the stream of $FC(t)$ matrices, we extracted $M = N(N-1)/2$ time series of pairwise FC couplings given by the entries $FC_{ij}(t)$ for all pairs of regions i and j with $i < j \leq N$. We used a window-size of $\tau = 16$ TR (~ 31 s) with a window step of one TR (1.94 s). The entries of the meta-connectivity matrix MC were given by the conventional Pearson correlation values:

$$MC_{ij,kl} = \text{CC}(FC_{ij}(t), FC_{kl}(t))$$

We compiled these correlation entries into a format that allowed us to easily identify the pair of links involved into each meta-link and the participating brain regions. That is, we built MC matrices of (N^2-N) -times- (N^2-N) size, where different rows corresponded to different directed pairs of regions – i.e. both the pair (i,j) and the pair (j,i) were included – and only links corresponding to self-loops – i.e. of the type (i,i) – were excluded. The price to pay for this choice of clarity was to introduce redundancy among MC matrix entries, since:

$$MC_{ij,kl} = MC_{ji,kl} = MC_{ij,lk} = \dots = MC_{kl,ij} = \dots MC_{lk,ji}$$

For the sake of computational efficiency, however, we computed only $P = M(M-1)/2$ independent Pearson correlations between pairs of possible FC link time series $FC_{ij}(t)$ and $FC_{kl}(t)$, with $i < j$, $k < l$, $i \leq k$, $j < l$ and copied this inter-link correlation value into the eight degenerate MC matrix entries.

Besides the strengths $MC_{ij,kl}$ of individual meta-links, we also computed integrated meta-connectivity strengths for individual links

$$MC(ij) = \sum_{kl} MC_{ij,kl}$$

This quantity, depending uniquely on the two indices i and j , and not anymore on the four indices i, j, k and l , measures the total strength of all inter-link interactions involving a given link (ij) . We could compute an analogous integrated strength for each brain region i :

$$MC(i) = \sum_{kl} MC_{ik,il}$$

We limited in this case the sum to ‘*trimer*’ meta-links only, having the considered region i as ‘root’. We call ‘*trimers*’ these special meta-links MC_{ikil} which give the strength of interaction between two functional links (ik) and (il) that share the common root region i . Trimer meta-links involve therefore a total number of three different brain regions. Trimers are thus distinct from general *tetramer* meta-links, which involve two links touching a total of four different brain regions.

In the adopted format, the MC matrix can be considered as the adjacency matrix of a graph whose nodes are FC links. Thus communities of temporally co-varying FC links can simply be evaluated by extracting node-based communities out of the MC matrix. To extract MC modules, we adopted, as for the modular structure of $FC(t)$ matrices, a standard Louvain algorithm, and selected the best modularity solution out of 500 independent runs. We extracted the modular structure in Fig. 4A out of the group average of single subject MC matrices taken over the ‘Young’ group of subjects (see above the ‘Subjects’ subsection for information about this group’s composition).

We found that negative strength meta-links are particularly informative about age. Hence, we defined

$$\text{neg-MC} = \sum_{ij,kl} |MC_{ij,kl}| \cdot \theta(-MC_{ij,kl})$$

where $\theta(x)$ denotes the Heaviside function which is equal to 1 if $x \geq 0$ and equal to 0 otherwise. In this way, neg-MC gives the sum of the absolute values of all the negative entries of the MC matrix. Growing neg-MC denotes the emergence of frustration and conflicting inter-link influences, and, hence, an increasing ‘viscosity’ of the FCD flux.

Age prediction via linear regression. We took into account a large number of different possible features as potential predictors of age. These predictors included the strengths of structural connectivity links SC_{ij} or of time-averaged functional connectivity links FC_{ij} , their variance over time $\sigma(FC_{ij})$ and their integrated meta-connectivity strength $MC(ij)$. We also considered node-based features, such as the total strengths of a region under structural connectivity and functional connectivity, i.e. $SC(i)$ and $FC(i)$, and regional trimer meta-connectivity strengths $MC(i)$. As shown in Fig. S6, for every possible brain region i and link (ij) , we tested whether these quantities correlated with subject age and whether correlations were significant (via bootstrap with replacement, $p < 0.05$).

We performed age-prediction based on different sets of features. As predictor sets we used quadruplets of: SC_{ij} 's, FC_{ij} 's, $\sigma(FC_{ij})$'s or $MC(ij)$'s; and, finally, mixed quadruplets composed of exactly one SC_{ij} , one FC_{ij} , one $\sigma(FC_{ij})$ and one $MC(ij)$ features. For each of these types, we tested all the possible feature quadruplets, keeping track of their performance in age-predictions and then isolating the best quadruplet of each type.

For each chosen set of predictor features, prediction performance was evaluated following a cross-validation procedure. First, we randomly split the subjects into two age-balanced halves by including within each of the halves subjects belonging to all four age quartiles in equal number. One half was designated as the 'training' set; the second half was designated as the 'testing' set. Then, we fitted a linear relation between age and the chosen predictor set (standard least-square procedure) based on the subjects in the training set, and evaluated this linear relation over the subjects in the testing set to extrapolate their age. Subsequently, we compared the predicted age with the actual age, and evaluated absolute errors of prediction $|age_{real} - age_{predicted}|$ and averaged them over the testing set to obtain the mean absolute error (MAE). Distributions of the expected MAE were then built by replicating 1000 times the random splitting of the overall sample into training and testing subsets. The boxplot in Fig. 6A shows the median, inter-quartile range and 95% confidence interval for the MAE distributions associated with the best quadruplet of links for each of the predictor set types. The best predictor sets achieving these performances are detailed in Figs. 6B-C.

Discrimination into age-classes. Next to the best features for each of the predictor types, we studied the general performance of all the different features in a simpler task, in which only the age-class of a subject had to be predicted, rather than her/his actual age. Subjects were split into two classes, age 'older than median' (the target class) and age 'higher than median'. Again subjects were separated into training and testing sets. A linear regression was then performed over the training set only. Ages for the testing set were predicted using these fitted linear relations. Finally, an age class was inferred depending on whether the predicted age was lower or higher than the actual whole sample median, used as a discrimination threshold. We evaluated performance metrics in terms of *sensitivity* (a.k.a. recall):

$$\text{Sensitivity} = \frac{TP}{TP + FN}$$

and *precision*:

$$\text{Precision} = \frac{TP}{TP + FP}$$

where TP denotes the number of true positives, FP the false positives and FN the false negatives in age-class discrimination over the testing set. Distributions of Sensitivity and Precision were finally built for each predictor quadruplet, by repeating the random split into training and testing subsets 1000 times. Fig. 6D depicts the joint histograms of the achieved median Precision and Sensitivity pairs sampled over all considered quadruplets of predictors (4x SC_{ij} , 4x FC_{ij} , 4x $\sigma(FC_{ij})$, 4x $MC(ij)$ and four mixed types).

Data and software availability

All anonymized datasets and custom analysis scripts will be made available on demand to the lead contact after publication of the manuscript. For the availability of structural and functional imaging data pre-processing pipelines see (Schirner et al., 2015). For the DFA toolbox see (Ton & Daffnersthofer, 2016).

Supplemental information

Supplemental figures

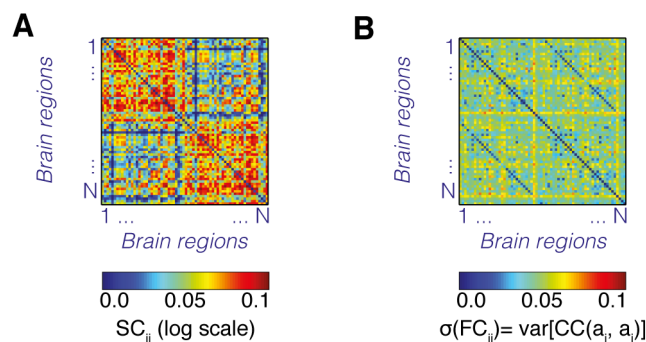


Fig. S1. Additional features affected by brain aging. Besides FC and FCD features we also monitored the changes through the human adult lifespan of additional features. (A) We extracted SC matrices via DSI using the same parcellation adopted for FC and FCD. Here we show a SC matrix averaged over the whole sample. (B) We also investigated the temporal variance of every FC link independently, ignoring inter-link covariances, unlike in MC analysis. Here we show a $\sigma(\text{FC})$ matrix (evaluated with a sliding window size of $\tau = 31$ s, as for the MC matrices in Fig. 4) averaged over the whole sample.

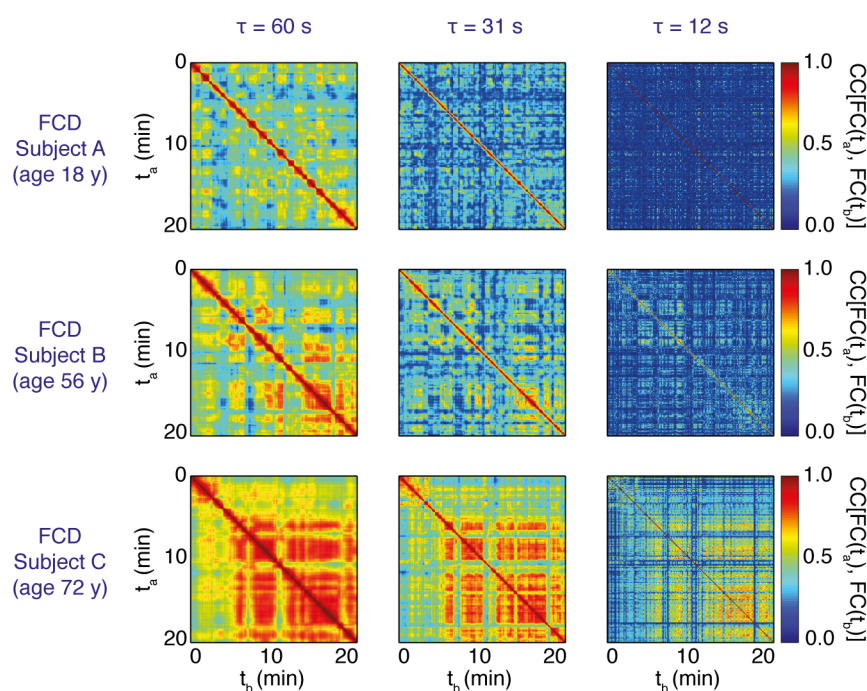


Fig. S2. FCD matrices for different sliding window sizes. FCD analyses for the same subjects considered in Fig. 2A are shown, for three different FCD window sizes τ -s. To simplify comparison, in the left column we reproduced the same FCD matrices already presented in Fig. 2A. Blocks of relatively elevated inter-network correlation corresponding to FCD knots were clearly visible for all time scales and ages.

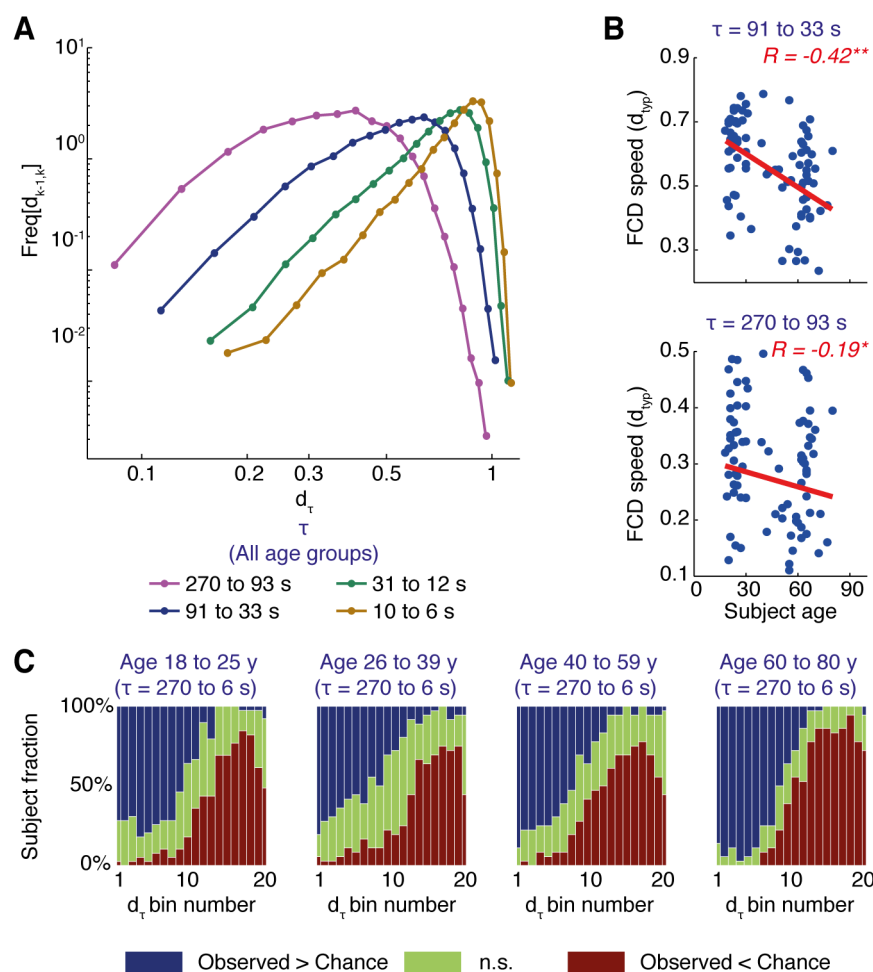


Fig. S3. Additional information on FCD step length distributions. (A) Distributions of FCD step lengths sampled over all subjects (all ages mixed), for different ranges of sliding window sizes. The first three ranges chosen to pool time-scales ('long': $270 \text{ s} \geq \tau \geq 93 \text{ s}$; 'normal': $91 \text{ s} \geq \tau \geq 33 \text{ s}$; 'short': $31 \text{ s} \geq \tau \geq 12 \text{ s}$) were set to guarantee that within each group roughly the same overall number of d_{τ} values was sampled. For comparison, we also show the case of ultra-short window sizes ($10 \text{ s} \geq \tau \geq 6 \text{ s}$). A typical FCD speed peak could be extracted for every time-scale group but that depended on the pool of used window-sizes. Fatter right tails developed for shorter window sizes. (B) For longer sliding window sizes, the typical FCD speed continued to anti-correlate with age (bootstrap with replacement, $p < 0.05$). The effect size, however, was smaller than for the faster sliding window size adopted in Figure 2C. (C) Single-subject d_{τ} distributions displayed an over-representation of short step lengths and an under-representation of long step lengths with respect to chance level for all age-groups and all time-scales. To test this, we performed a bin-by-bin comparison between empirical and null-hypothesis distributions of d_{τ} . We matched the results of these comparisons for all window sizes (here, one-by-one, no longer pooled), by collating them bin-by-bin according to the ordinal rank of the bins. The results of this comparison are shown for different age groups. In all cases, the relatively shorter (longer) step length bins were associated with larger (smaller) than chance level frequencies (blue or red, respectively). This separation between over- and under-representation for different step length ranges became 'crisper' with increasing age, as denoted by a reduced fraction of bin-by-bin non-significant comparisons (green).

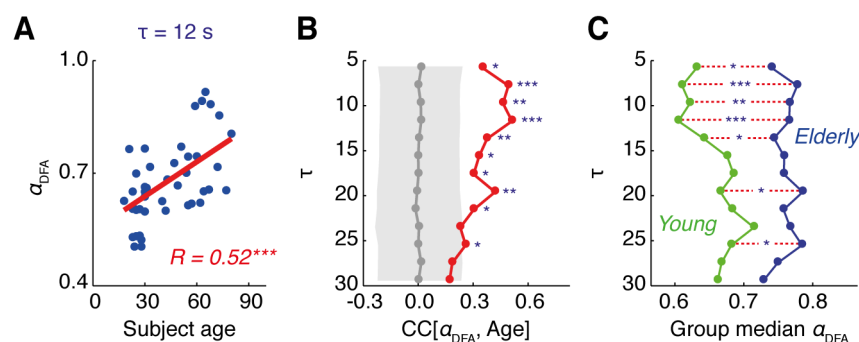


Fig. S4. Additional information about Detrended Fluctuation Analysis of FCD.

(A) Scaling exponents α_{DFA} extracted from a Detrended Fluctuation Analysis of the sequence of FCD step lengths correlated positively with age at the single subject level (scatter plot for a FCD window-size of $\tau = 12$ s). (B) Correlations between α_{DFA} and subject age were significantly positive for all the tested FCD window-sizes up to 27 s (*, $p < 0.05$; **, $p < 0.01$; ***, $p < 0.001$; permutation test). The grey curve corresponds to the expected correlation in the null hypothesis case of no association (shaded interval, 95% confidence interval under permutation test). (C) Group averages of α_{DFA} for young and elderly subjects (18-25 yrs, max $N = 13$; 57-80 yrs, max $N = 12$) as a function of the adopted FCD window-size τ . Inter-group comparison were significant for several short windows lengths (meaning of *, **, *** as in panel B; U Mann-Whitney test). Note that compared groups had different sizes for different τ values, depending on how many subjects were retained as showing a genuine power law scaling in the DFA plot by the (Bayesian) model selection step. Up to $\tau < 29$ s, at least $N = 35$ out of 49 tested subjects with DFA ('rs only group') showed a genuine power-law scaling ($N = 46$ for $\tau = 12$ s, Fig. 2F and Fig. S4A).

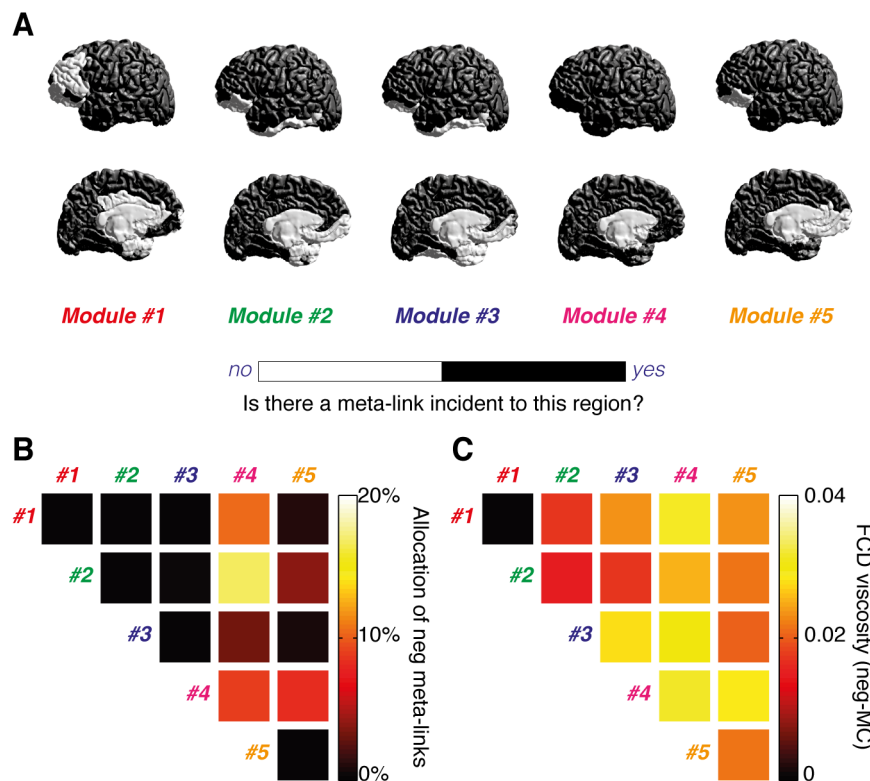


Fig. S5. Additional information on MC analysis. (A) MC modules were organized around different MC hub regions, as indicated by the MC trimer weight surfaces in Figure 4B. At the same time, all the modules had a brain-wide reach and are therefore highly distributed. In fact, for each brain region and for each MC module, it was possible to find a FC link that was incident to (meta-connected to) the area (the MC module) under consideration. (B-C) As shown in Figure 4D, negative meta-links developed with age. These negative meta-links were not equally distributed among MC modules and the largest fractions of them interconnect FC links in Module #4 (organized around orbito-frontal cortex) with FC links in Module #2 (fronto-parietal) or other modules, as indicated by the relative counts in panel (B), based on the group-averaged MC matrix over elderly subjects of Figure 4A. Equivalently, negative meta-connections originating from this Module #4 tended to have a larger absolute value, as shown in panel (C). In other words the FCD flux of regions in Module #4 was more ‘viscous’.

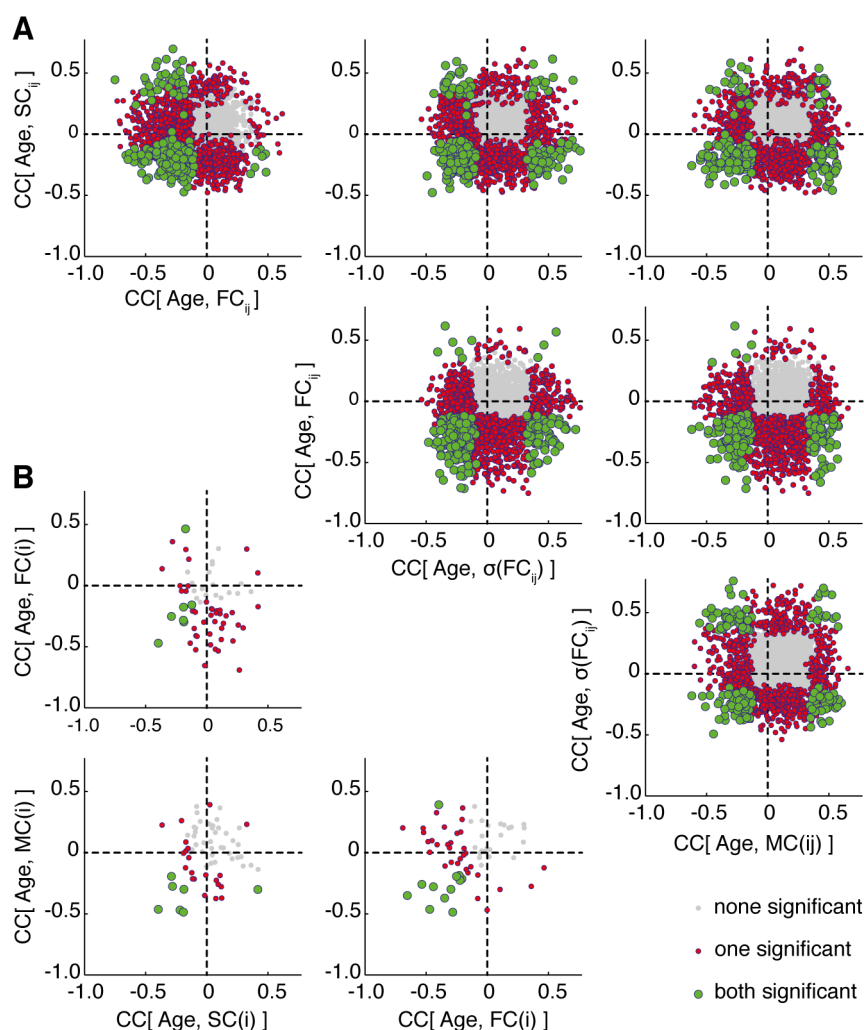


Fig. S6. Different types of predictor features yield non-redundant information about aging. (A) We considered individual pairs of regions i and j . For each of these pairs, we computed the correlation with age of: the strength of structural coupling, SC_{ij} ; the time-averaged value of functional connectivity, FC_{ij} ; the variance over time of time-resolved functional connectivity, $\sigma(\text{FC}_{ij})$; and the meta-connectivity strength of the considered FC link, $MC(ij) = \sum_{kl} MC_{ij,kl}$. We realized scatter plots of the correlations of these different predictor types with age for each possible pairwise link. (B) Next, we considered individual regions i and computed their regional SC strength, $SC(i) = \sum_j SC_{ij}$, their regional FC strength $FC(i) = \sum_j FC_{ij}$, and finally their regional meta-connectivity strength $MC(i) = \sum_{jkl} MC_{ij,kl}$. Analogously, we made scatter plots of their age correlations vs. each other for all the possible regions. In both panels (A) and (B), grey dots correspond to not significant correlations, red (or green) circles to cases in which at least one (or both, respectively) correlation coordinate is significant ($p < 0.05$, bootstrap with replacement). All the scatter plots in both panels (A) and (B) were unstructured, indicating that correlations with age for a predictor of a given type cannot trivially be anticipated from the knowledge of correlations with age for a different type of predictor, evaluated for the same region of pairwise link. It seems that SC, FC, $\sigma(\text{FC})$ and MC predictors generally did not contain redundant information about the aging process.

Supplemental table

Table S1. Used cortical parcellation and abbreviations

Abbreviation	Cortical Area
ENT	Entorhinal cortex
PARH	Parahippocampal cortex
TP	Temporal pole
FP	Frontal pole
FUS	Fusiform gyrus
TT	Transverse temporal cortex
LOCC	Lateral occipital cortex
SP	Superior parietal cortex
IT	Inferior temporal cortex
IP	Inferior parietal cortex
SMAR	Supramarginal gyrus
BSTS	Bank of the superior temporal sulcus
MT	Middle temporal cortex
ST	Superior temporal cortex
PSTC	Postcentral gyrus
PREC	Precentral gyrus
CMF	Caudal middle frontal cortex
POPE	Pars opercularis
PTRI	Pars triangularis
RMF	Rostral middle frontal cortex
PORB	Pars orbitalis
LOF	Lateral orbitofrontal cortex
CAC	Caudal anterior cingulate cortex
RAC	Rostral anterior cingulate cortex
SF	Superior frontal cortex
MOF	Medial orbitofrontal cortex
LING	Lingual gyrus
PCAL	Pericalcarine cortex
CUN	Cuneus
PARC	Paracentral lobule
INS	Insula

Parcellation based on Desikan et al. (2006).